Metabolic specialization drives reduced pathogenicity in *Pseudomonas aeruginosa* CF clinical isolates

Bjarke H. Pedersen [1], Filipa B. Simões [2], Ivan Pogrebnyakov [1], Martin Welch [3], Helle Krogh Johansen [1,2,4], Søren Molin [1] and Ruggero La Rosa [1,2#]

[1] The Novo Nordisk Foundation Center for Biosustainability, Technical University of Denmark, 2800 Kgs. Lyngby, Denmark

[2] Department of Clinical Microbiology 9301, Rigshospitalet, 2100 Copenhagen, Denmark

[3] Department of Biochemistry, University of Cambridge, CB2 1TN Cambridge, United Kingdom

[4] Department of Clinical Medicine, Faculty of Health and Medical Sciences, University of Copenhagen, 2200 Copenhagen, Denmark

Address correspondence to Ruggero La Rosa, rugros@biosustain.dtu.dk

Abstract

Metabolism provides the foundation for all cellular functions. During persistent infections, in adapted pathogenic bacteria it functions radically differently compared with more naïve strains. However, whether this is simply a necessary accommodation to the persistence phenotype or if metabolism plays a direct role in achieving persistence in the host is still unclear. Here, we characterize a shift in metabolic functions aligned with a persistence phenotype occurring in eight infection scenarios of *Pseudomonas aeruginosa* colonization of people with cystic fibrosis. We identify clinical mutations in the key metabolic enzyme pyruvate dehydrogenase leading to a host specialized metabolism together with a lower virulence and immune response recruitment. This is mediated by impaired type III secretion system activity and by secretion of the antioxidant metabolite, pyruvate. These results provide evidence for the direct adaptiveness of metabolism during a persistent infection and its intrinsic role in supporting pathogenicity.

Introduction

Metabolism of bacterial pathogens is a central process involved both in cell duplication and in virulence. In several infections, nutrient composition of the host microenvironment provides an environmental cue for bacterial pathogens to activate their virulence repertoire [1]. For instance, abnormalities in calcium homeostasis, nutrient limitation or change in pH signals activation of the type III secretion system (T3SS) cascade in several bacterial species [2–5]. Similarly, metabolism dependent processes such as biofilm production and mucoidy provide shielding from antibiotics and immune cells, and are generally associated with worse prognosis [6–8]. Furthermore, crosstalk between bacteria and immune cells through exchange of bacterial and host metabolites has additionally revealed the importance of metabolism in determining the outcome of an infection [9–11].

However, metabolism is not a static function; it dynamically changes to support cell growth and virulence specifically for each host and type of infection. For example, clinical strains of *Pseudomonas aeruginosa* that infect people with cystic fibrosis (pwCF), have been shown to modify their metabolic preference to accommodate to the specific nutrient composition of the airways [12,13]. Auxotrophy, specialized assimilation of carbon sources, secretion of high

53 value metabolites and differential oxygen requirements of adapted clinical strains ensure
54 appropriate functionality of the cell and support the phenotype requirements in the host [14].

55 In persistent infections, genetic variants with high antibiotic resistance, tolerance to other
56 stresses, host and immune evasion capabilities or low virulence are specifically selected for
57 since they provide higher within-host fitness [16–18]. However, it is still unclear if and how
58 metabolic specialization directly contribute(s) to persistence [12,21]. Few examples of laboratory
59 studies in *P. aeruginosa* and *Escherichia coli* have suggested the involvement of specific
60 metabolic mutations with changes in antibiotic susceptibility and virulence [22–26]. However,
61 limited knowledge is available on their relevance and purpose in clinical isolates during an
62 infection. Moreover, the extent to which metabolic specialization *per se* provides a specific
63 fitness advantage or if it is merely a consequential metabolic adjustment caused by other
64 essential phenotypes, still remains unknown. Furthermore, the specific selective forces (for
65 example antibiotic treatment or the immune system) leading to metabolic specialization are
66 still largely uncharacterized.

67 By analyzing in detail, the metabolic and proteomic profiles of clinical strains of *P. aeruginosa*
68 at different stages of host adaptation from pwCF, we identified distinct metabolic
69 configurations characterized by CF-specific nutrient assimilation and secretion patterns. This
70 was caused by changes in proteome allocation and metabolic mutation. Additionally, we
71 characterized a specific metabolic specialization involving the pyruvate dehydrogenase
72 complex (PDHc) which is essential for the processive flux of pyruvate through central carbon
73 metabolism. Surprisingly, recombinant strains containing single mutations in the PDHc show
74 decreased infection capabilities and immunogenicity in an Air-Liquid Interface (ALI) infection
75 model system. These strains display a chronic-like phenotype and an increased secretion of
76 pyruvate, which is an important scavenger of reactive oxygen species (ROS) and has known
77 anti-inflammatory properties [27–29]. Importantly, these mutations are widespread in clinical
78 isolates of *P. aeruginosa* suggesting that adaptation to the host environment and metabolic
79 specialization might be specifically selected for during the early stages of an infection, thereby
80 limiting host-dependent inflammation. Altogether these results provide a rationale for
81 metabolic specialization during CF airway infections.

82

83 **Results**

84 *Growth rate reduction as proxy for within-host adaptation*

85 To gain insight on the metabolic adaptation occurring in *P. aeruginosa* clinical isolates during
86 the infection of pwCF, we selected pairs of early (first *P. aeruginosa* isolated from the person)
87 and late clinical isolates, longitudinally isolated from eight different pwCF and belonging to
88 distinct clone types (> 10.000 SNPs difference) (Fig. 1a). Reduced growth rate was used as
89 proxy for within-host evolution, enabling us to assemble a diverse and variegated collection
90 of clinical isolates spanning between 1.4 and 7 years of within-host evolution (Table S1). When
91 grown in SCFM medium (which has been formulated to resemble the CF mucus composition
92 [15]), early isolates showed a high growth rate comparable to the reference strain, PAO1.
93 Conversely, late isolates showed a 2.2- to 5.1-fold reduction in growth rate, in addition to a
94 halved maximal optical density (paired t test, P = 0.002) (Fig. 1a-b). Moreover, some late
95 isolates were unable to grow in minimal medium in presence of single carbon sources such as
96 glucose, lactate or succinate, suggesting a certain level of metabolic constraint (Fig. 1c).

97 Despite belonging to distinct clone types, a certain degree of phylogenetic convergence is
98 shown by early and late strains, since they tend to cluster closely within each group (early or
99 late) rather than by their clone type (Fig. 1d). The distribution of mutations either
100 accumulated or reverted during within-host evolution differs between clone types confirming
101 different evolutionary trajectories in each host, including hypermutation events (Fig. 1e and
102 Supplementary Data 1). However, mutated genes are similarly enriched between clone types
103 (pyoverdine biosynthetic process for Gene Ontology (GO) categories and bacterial secretion
104 system and porphyrin metabolism for Kyoto Encyclopedia of Genes and Genomes (KEGG)
105 categories) confirming, as also shown in several other investigations [19,20], conserved targets of
106 within-host evolution between infection scenarios (Fig. 1f).

107

108 *Within-host evolution selects for specialized metabotypes*

109 To evaluate the degree of metabolic specialization of the selected clinical isolates, dynamic
110 exo-metabolomics was performed on cells growing in SCFM (Supplementary Data 2). PCA of
111 the extracellular metabolomes reveals the presence of three distinct late specialized
112 metabolic configurations, here defined as “metabotypes” (DK15 and DK55 metabotype 1;

113 DK12 metabotype 2; DK03, DK13 and DK36 metabotype 3). In these metabotypes, late
114 isolates separate from each respective early isolate and from the rest of the non-adapted
115 metabotypes (Fig. 2a). While PCA emphasizes the largest differences in the metabolome
116 profiles, hierarchical cluster analysis clearly separates early from late strains indicating a
117 certain degree of metabolic specialization in all late isolates (Fig. 2b). Indeed, both the
118 hierarchy of assimilation (metabolites half-life, OD_{50}) and the secretion of metabolites differs
119 between early and late isolates (Fig. 2c-d). Specifically, metabotype 1 shows reduced
120 assimilation of Lys, Gly, Ile, Leu, Phe, Thr, Tyr and Val and secretion of pyruvate by strain DK55
121 late; metabotype 2 shows increased assimilation of glucose, Ala, Asp, Glu, Gly, Pro, Ser, Arg
122 and His, and secretion of high amount of pyruvate; and metabotype 3 shows increased
123 assimilation of glucose and lactate, differential assimilation of Ala, Asp, Glu, His and Pro and
124 secretion of pyruvate by strain DK36 late (Fig. 2c-d). Late DK13, DK36 and DK41 strains secrete
125 a low concentration of formate whereas all late isolates secrete acetate, albeit at different
126 concentrations and with different growth-dependent profiles (Fig. 2d). Unsurprisingly, the net
127 balance between assimilated and secreted metabolites (total mM) varies between early and
128 late strains (Fig. 2e), which positively correlates with the lower biomass of the late isolates
129 (Pearson's r = 0.9; P = 0.0023) (Fig. 1b and 2e). This suggests either a specific metabolic
130 configuration for the late isolates, the objective of which is not biomass accumulation, or an
131 apparent inefficient metabolism.

132

133 *Changes in proteome allocation supports the metabolic specialization of clinical isolates*

134 To evaluate the contribution of the proteome composition to the metabolic specialization of
135 clinical strains, we performed whole cell proteomics to compare protein profiles between
136 strains. Of the 2061 proteins identified, 740 proteins were differentially expressed in at least
137 one comparison (early *vs* PAO1 or late *vs* early) (Supplementary Data 3). Similar to the
138 metabolomic analysis, PCA separates late from early proteomes suggesting that changes in
139 metabolite profiles might be rooted in the proteome (Fig. 3a, b). Most of the early and some
140 of the late proteomes colocalize with the reference strain PAO1 indicating little or no changes
141 in proteome allocation (Fig. 3a, b). However, proteomes of the late isolates of lineages DK12,
142 DK17, DK36, and DK55 separate from the respective early strains forming a cluster of adapted
143 proteomes (Fig. 3a, b). Notably, DK03 strains form an independent cluster, indicating a lineage

144 specific proteome signature which might depend in the already reduced growth rate of the
145 early isolate (Fig. 1a and 3a, b).

146 A similar result is obtained when performing hierarchical clustering analysis specifically on the
147 235 differentially expressed proteins between late and early strains belonging to the Clusters
148 of Orthologous Groups (COG) categories involved in metabolism. The adapted metabotypes
149 DK12, DK36 and DK55 and DK17 (cluster B) separate from the naïve metabotypes (cluster A)
150 supporting the hypothesis that metabolism specialization is likely rooted in changes in
151 expression of proteins involved in cellular metabolism (Fig. 3c). Notably, cluster B is
152 characterized by a higher number of differentially expressed proteins in the categories of
153 amino acids and lipid metabolism, and energy production and conversion relative to cluster
154 A (Fig. 3d and Fig. S1a). Similarly, several categories of proteins involved in the metabolism of
155 amino acids, fatty acid and sugars are statistically enriched in naïve and adapted clone types
156 (Fig. S1b) providing a molecular explanation for the altered hierarchy of assimilation of the
157 carbon sources and the reduced growth rate of the late adapted metabotypes (Fig. 2c, d).

158 Albeit late strains of DK12, DK36, DK55 belong to different metabotypes, their proteomes
159 move in the same direction (Fig. 3a-c). This indicates that largely similar proteomes can
160 sustain distinct metabolic configurations which ultimately depend on the metabolic fluxes
161 thorough specific pathways and on their regulation. Moreover, proteome adaptation can be
162 achieved without rewiring of metabolism as shown by strain DK17 which belongs to cluster B
163 (Fig. 3a-c), but does not present any major metabolic rewiring (Fig. 2a, b).

164 Interestingly, several enzymes belonging to the Entner-Doudoroff/Embden-Meyerhof-
165 Parnas/Pentose Phosphate (EDEMP), and tricarboxylic acid (TCA) cycle pathways are up-
166 regulated in the early and late strains relative to PAO1, indicating a specific and convergent
167 configuration of central carbon metabolism enzymes that are optimal for exploiting the
168 airway's resources (Fig. 3e and S2). For example, our metabolomic data show that several late
169 strains (belonging to metabotypes 2 and 3) exhibit increased glucose assimilation, which is in
170 agreement with the increased expression of pathways involved in glucose assimilation
171 (enzymes 3, 11, 12, 18) (Fig. 3e). Similarly, the fumarate hydratase (enzyme 33) together with
172 the enzymes involved in Trp, Phe and Tyr catabolism (enzymes 65 and 66) show increased
173 expression, likely to better accommodate the increased assimilation of amino acids which are
174 catabolized through the TCA cycle (Fig. 3e). This hypothesis is corroborated by the changes in

175 expression (both increased and decreased) in late *vs* early strains of several enzymes involved
176 in amino acids, glucose, and lactate catabolism and of their respective transporters (Fig. 3e).
177 This proteome configuration supports the hypothesis that overflow of amino acids through
178 central carbon metabolism, might be the cause of increased pyruvate secretion in late strains
179 of DK12, DK36 and DK55 (Fig. 2d and 3e).

180

181 *Changes in virulence traits during within patient evolution*

182 Analysis of the differentially expressed proteins enriched when comparing late *vs* early
183 isolates shows that most of the changes are directed toward adaptation to the infection
184 environment, and especially to redox balance and virulence (Fig. 4a and S1b). Indeed, the
185 categories of proteins showing expression changes in most of the lineages are phenazine
186 biosynthesis (KEGG) and secondary metabolite(s) biosynthetic process (GO) which are deeply
187 connected with cell homeostasis, metabolism and virulence [30,31]. Not surprisingly, several
188 clone types harbour mutations in genes belonging to the pyoverdine biosynthetic process
189 (GO) category (Fig. 1f), and several mutated genes shared between metabotypes belong to
190 the COG category of secondary metabolites biosynthesis, transport and catabolism (Fig. S1b).
191 Interestingly, several changes in protein expression are already shown by early strains relative
192 to PAO1 indicating a different response of clinical strains to the airway-like conditions of the
193 SCFM medium (Fig. 4a). Specifically, early strains show increased expression of proteins
194 involved in alginate production, hydrogen cyanide (HCN), phenazine biosynthesis and PQS
195 (*Pseudomonas* quinolone signal), and decreased expression of proteins involved in flagella
196 biogenesis, lipopolysaccharide (LPS) O-antigen metabolism and pyoverdine production, which
197 are all hallmarks of an acute phenotype (Fig. 4b). Instead, the adapted metabotypes, and
198 specifically strains belonging to cluster B, show convergent up-regulation of proteins related
199 to alginate, phenazine, PQS and the type VI secretion system (T6SS) suggesting an active role
200 of metabolism in virulence regulation and the chronic infection phenotype (Fig. 4c and S3).
201 Interesting, the DK12 late strain also shows lower expression (-1.5-fold) of the type III
202 secretion system (T3SS) secreted factor ExoT, the activity of which prevents phagocytosis and
203 induces cytoskeletal reorganization and host cell apoptosis [32,33]. Overall, the identified pattern
204 suggests a reduced immunogenicity of the clinical strains relative to PAO1, and an even

205 greater reduction in the late isolates. This is in line with their persistence during CF airway
206 infections.

207

208 *aceE and aceF mutations leads to metabolic specialization and impaired virulence*

209 Screening for mutations which could explain the metabolic specialization of the late isolates
210 and the lower expression of virulence determinants, led to the identification of mutations in
211 genes encoding the pyruvate dehydrogenase complex (PDHc), *aceE* and *aceF*, in late strains
212 of DK12 and DK36, respectively (Supplementary Data 1). The PDHc catalyses the conversion
213 of pyruvate into acetyl-CoA, connecting sugar metabolism to the TCA cycle (Fig. 3e).
214 Interesting, the *aceE* and *aceF* genes are candidate pathoadaptive genes and their *in-situ*
215 expression is reduced in sputum samples collected from chronically-infected pwCF [19,34]. This
216 suggests an undescribed role of the PDHc activity during infection.

217 To evaluate the contribution of *aceE* and *aceF* mutations to the bacterial phenotype,
218 independent of the underlying historical contingency of the clinical strains, we generated
219 recombinant PAO1 derivative strains containing the +TCCC duplication (position 813) in *aceF*
220 from the late DK12 strain, and the T→C SNP (position 551) in *aceE* from the late DK36 strain
221 (Fig 5a). The *aceF* mutation leads to a frameshift of translation starting from Lys 273, whereas
222 the *aceE* mutation leads to a Phe→Ser amino acid change. The recombinant *aceE* and *aceF*
223 mutant strains show reduced growth rate and increased secretion of pyruvate similar to that
224 of the DK12_L and DK36_L late strains (Fig. 1a, 2d and 5c). The *aceE* mutant strain shows a
225 milder phenotype (a smaller reduction in growth rate reduction and lower pyruvate secretion)
226 compared with the *aceF* mutant strain, suggesting partial functionality of the PDHc. Indeed,
227 supplementing acetate to the bacterial culture to replenish the pool of acetyl-CoA, fully
228 restored the growth phenotype of the *aceE* strain, whereas it only partially restored growth
229 in the *aceF* mutant strains (Fig. 5b). This confirms a much more significant effect of the *aceF*
230 mutation on the activity of the PDHc. Surprisingly, phenotypes such as biofilm formation,
231 motility, redox susceptibility, pyoverdine production and antibiotic susceptibility, were not
232 affected much, with no differences observed between the PAO1 wild-type strain and the *aceE*
233 and *aceF* mutant strains, except for a slight decrease in twitching motility and mildly increased
234 tobramycin susceptibility (Fig. S5). Screening for other *aceE* and *aceF* mutations in our strain

235 collection, we identified the presence of 18 different mutations (4 indels and 14 SNPs of which
236 3 silent) supporting the hypothesis that modulation of the PHDc might be selected for
237 specifically during airway infections for reasons other than antibiotic resistance (Fig. S4).

238 To characterize the effect of the *aceE* and *aceF* mutations more broadly, we performed whole
239 cell proteomics on the *aceE* and *aceF* recombinant strains (and on the PAO1 progenitor) in
240 presence and absence of acetate. In total, we quantified 3246 proteins and identified 449 as
241 differentially expressed in at least one comparison of either mutant *vs* wt strain or of mutant
242 strain in presence *vs* absence of acetate (Supplementary Data 4). In the absence of acetate,
243 the proteomes of the *aceE* and *aceF* mutant strains cluster in different quadrant compared
244 with that of PAO1. PC1, which encompasses >50% of the variance in the dataset, separates
245 the *aceF* strain proteome from that of PAO1, whereas less than 20% of the variance separates
246 the proteome of the *aceE* strain from that of PAO1 along PC2 (Fig. 5d). As previously reported,
247 the supplementation of acetate benefits both the *aceE* and *aceF* strains, with both proteomes
248 moving closer to that of PAO1 (Fig. 5d). This effect is accentuated in the *aceF* mutant strain
249 where the supplementation with acetate decreases the number of differentially expressed
250 proteins by more than half (from 301 to 126) (Fig. 5e). Not surprisingly, several enzymes
251 involved in central carbon metabolism and amino acid catabolism, and specifically those
252 involved in pyruvate and acetyl-CoA metabolism (lactate dehydrogenase (41), acetyl-
253 coenzyme A synthetase (6), citrate synthase (28)) are up-regulated in the *aceF* mutant strain
254 whose expression returns to wild-type levels following the addition of acetate (Fig. 5f and
255 S6a). As shown for the clinical isolates DK12_L and DK36_L, the categories of proteins
256 involved in amino acid and lipid metabolism, and energy conversion presented the highest
257 number of differentially expressed proteins (Fig. S6b). Similarly, proteins involved in terpene,
258 propionate, isoprenoid and branched-chain amino acids (which are directly connected to
259 pyruvate and acetyl-CoA metabolism) where statistically enriched in the *aceF* mutant strain
260 indicating a reorganization of both central and peripherical pathways to cope with reduced
261 synthesis of acetyl-CoA (Fig. S6c). Importantly, the *aceE* and *aceF* mutant strains show
262 increased expression of proteins involved in alginate production and T6SS, and reduced
263 expression of proteins involved in the T3SS, including the secreted factor ExoT (strain *aceF*
264 and DK12_L) (Fig. 5g and Supplementary Data 4). This indicates that the *aceE* and *aceF*

265 mutations are the leading cause of the expression profile of virulence determinants shown by
266 the late clinical isolates of DK12 and DK36 (Fig. 4, 5g and Supplementary Data 4).

267

268 *Pyruvate dehydrogenase mutations modulate pathogenicity in ALI culture infections*

269 To test whether the reduced expression of virulence determinants in the *aceF* and *aceE*
270 mutant strains leads to reduced infectivity, we performed host-bacteria infections using an
271 ALI infection model system composed of mucociliated differentiated airway epithelial cells
272 and the recombinant *aceF* and *aceE* mutant strains. Overall, the *aceF* mutant strain displayed
273 a broad suppression of virulence, including reduced epithelium damage and innate immune
274 recognition during the infection (Fig. 6). The transepithelial electrical resistance (TEER) which
275 quantifies the integrity and permeability of the epithelial layer, LDH release which quantifies
276 the epithelium cellular damage, and the bacterial count which quantifies the growth and
277 penetration of the bacteria through the epithelium to the basolateral side of the ALI
278 transwells, all showed reduced values after 14 hours of infection when compared with the
279 PAO1 reference strain (Fig. 6a). This is in line with the behaviour of a *ΔpscC* mutant strain
280 defective in T3SS which shows a severely reduced virulence (Fig. 6a). By contrast, the *aceE*
281 strain, elicited similar epithelial damage to PAO1, indicating that the mutation does not
282 influence bacterial penetration (Fig. 6a). This is consistent with the proteomic analysis
283 showing no significant differential expression of proteins involved in the T3SS in this strain
284 (Fig. 5f). However, both the *aceE* and *aceF* strain together with the *ΔpscC* mutant strain elicit
285 lower interleukin 8 (IL-8) release which is secreted by the epithelial cells, and it is necessary
286 for the recruitment of the immune system at the site of infection (Fig. 6b). Such reduced
287 recognition from the epithelial layer of the *aceE* and *aceF* strains might depend on the
288 secretion of bacterial pyruvate, which is known to mediate the inflammatory response in both
289 the epithelium and the immune cells [28,29,35]. These results are corroborated by confocal
290 microscopy data, which show a similar colonization profile on the airway epithelium of the
291 PAO1 and *aceE* strains, and of the *aceF* and *ΔpscC* respectively. This mechanism of reduced
292 cellular damage and reduced immunogenicity seems not to depend on the growth defect
293 associated with the *aceF* strain, since the *ΔpscC* strain shows comparable aggressiveness to
294 the *aceF* mutant strain but a wild type-like growth rate.

295 Importantly in our longitudinal collection of clinical strains of *P. aeruginosa*, 20 lineages (clone
296 types in specific pwCF; 89 isolates) harbour mutations in the *aceE* and *aceF* genes and/or
297 additional mutations in T3SS genes. In 9 lineages, PDHc mutations are present alone or
298 anticipate additional T3SS mutations. In 7 lineages, T3SS mutations precede PDHc mutation
299 or both systems are mutated at the same time (4 lineages) already in the first isolate of the
300 lineage (Fig. S7). Altogether these results suggest a role for the *aceE* and *aceF* mutations prior
301 those on the T3SS. Moreover, they provide direct evidence of the contribution of metabolism
302 to bacterial virulence and to the persistence phenotype.

303

304 **Discussion**

305 Metabolism constitutes a central process which is specifically regulated and optimized
306 according to the nutritional resources available and the phenotypic requirements of the cell.
307 Several studies have shown that metabolic specialization occurs in clinical isolates of *P.*
308 *aeruginosa* [14]. However, little is known about whether this metabolic specialization is simply
309 an accommodation for other significant fitness gains, or whether it is specifically selected for
310 to enable increased persistence in the host.

311 By analysing different clinical isolates of *P. aeruginosa*, we show that all infection lineages
312 underwent a substantial metabolic rewiring associated with changes in proteome allocation
313 driven by mutations in metabolic genes. Adapted strains harbouring mutations in the genes
314 encoding the PDHc (*aceE* and *aceF*) are characterized by a chronic-like phenotype (T3SS down-
315 regulation, up-regulation of T6SS, phenazines and alginate biosynthetic pathway and slow
316 growth) suggesting selective advantages in the host [18]. Moreover, adapted strains secrete
317 high amount of pyruvate, which is an important mediator of inflammation in the host [28].
318 Testing aggressiveness in an ALI culture model confirmed that the *aceE* and *aceF* mutant
319 strains elicit less stimulation of the immune system and reduced epithelial penetration,
320 respectively. Such reduced aggressiveness in the *aceF* mutant strain appears to be mediated
321 by reduced expression of the T3SS effector ExoT, which induces apoptosis in host cells [32,33].
322 This result is consistent with previous studies showing that mutations in the PDHc-encoding
323 genes leads to repression of T3SS in *P. aeruginosa* [36,37]. Similarly, mutations in the *iso*citrate
324 lyase involved in the glyoxylate shunt in the TCA cycle has also been associated with reduced

325 T3SS activity proposing a direct correlation of metabolism to virulence [24]. As expected, the
326 DK15 late isolate in our collection shows reduced expression of the *iso*citrate lyase together
327 with suppression of ExoT exotoxin. Importantly, *aceE* and *aceF* mutations mostly precede
328 mutations in the T3SS-encoding genes, indicating a fundamental and broader role of the PDHc
329 mutations during evolution in the host. Moreover, the diversity of *aceE* and *aceF* mutations
330 indicates that the activity of the PDHc can be fine-tuned accordingly to the specific host and
331 consequently lead to different infection outcomes. Indeed, while the *aceE* mutant strain (SNP)
332 shows comparable aggressiveness to PAO1 but reduced recruitment of the immune system
333 (IL-8 secretion), the *aceF* mutant strain (indel) combines the effect of the reduced
334 aggressiveness and that of the reduced immune recruitment.

335 It is worth noting that pyruvate is a potent scavenger of ROS and, indeed, its use has been
336 suggested as an anti-inflammatory treatment in several diseases [27,35]. Due to the sustained
337 activation of neutrophils and other defects in the homeostatic processes of pulmonary
338 epithelia in CF airways, an abnormal flux of ROS is present which can be alleviated by the
339 bacterial pyruvate secretion [38]. Indeed, it has been shown that treatment of human lung
340 epithelial cells with pyruvate reduces the inflammatory response by reducing the production
341 of IL-8 [39,40], it induces a potent shutdown of the response to LPS in dendritic cells [41], and
342 reduces alveolar tissue destruction in COPD model system [42]. Similarly, inhibition of the PDHc
343 and redirection of the pyruvate flux has been suggested both as a potential anti-inflammation
344 therapy for chronic metabolic diseases [43], and as a cancer treatment [44]. Moreover, fine-tuning
345 of the flux through the mitochondrial PDHc in macrophages and dendritic cells is key for
346 regulating their polarization and thus the balancing between pro- and anti-inflammatory
347 responses [45–47]. LPS-induced polarization of macrophages is prevented by pharmacological
348 inhibition of pyruvate import into the mitochondria [48]. Moreover, flux through the PDHc
349 controls the production of the antibacterial cytokine itaconate [49–52].

350 The PDHc dysregulation seen in the clinical isolates may, therefore, serve as an alternative
351 mechanism for ensuring active pyruvate secretion and suppression of the immune system by
352 a mechanism of cross-feeding. This mechanism of host-pathogen crosstalk is evolutionary
353 beneficial in persistent infections since ROS produced in the CF airways might select for
354 metabolic specialization in *P. aeruginosa*. Moreover, the consequent reduced activity of the
355 T3SS limits epithelial damage to avoid any further inflammation. These combined

356 mechanisms can provide a rationale for the broad accumulation and maintenance of PDHc
357 mutations in our collection of *P. aeruginosa* clinical CF isolates and the reduced expression of
358 the PDHc in sputum samples [19,34]. Moreover, it suggests a highly complex and near universal
359 role of the pyruvate node in regulation of both host and pathogen (and their respective
360 functions *in vivo*) through a conserved central metabolite. Such a mechanism might be used
361 years before the development of antibiotic resistance, therefore being of high relevance for
362 the establishment of a chronic phenotype. Understanding specific mechanisms linking
363 metabolism, energy balance and virulence and most importantly how the relationship
364 between the host and the pathogen changes during an infection is of high relevance. Indeed,
365 it could provide new opportunities for improved and more efficient treatment (beyond the
366 classical antibiotic treatment) which are greatly needed.

367

368 **Methods**

369 *Strains and media*

370 The collection of clinical isolates used in this study is a subset of the collection published in
371 Marvig et al., (2015) and Bartell et al., (2019) [19,53]. The local ethics committee at the Capital
372 Region of Denmark (Region Hovedstaden) approved the use of the stored *P. aeruginosa*
373 isolates (registration number H-4-2015-FSP). For information about specific clinical isolates,
374 see Table S1.

375 For construction of *aceE* and *aceF* mutant strains, derivatives of pACRISPR were constructed
376 with the Uracil Specific Excision Reagent (USER) cloning [54]. The plasmids and primers used are
377 listed in Table S1 and S2 respectively. Target DNA fragments were amplified from gDNA of
378 clinical strains DK12 Late and DK36 Late using the Phusion U polymerase kit (Thermo Fisher
379 Scientific, USA). The resulting PCR products were treated with FastDigest DpnI enzyme
380 (Thermo Fisher Scientific, USA) and ligated with the USER® Enzyme (New England Biolabs,
381 USA). PCR was performed on random *Escherichia coli* DH5alpha colonies using OneTaq® 2X
382 Master Mix (New England Biolabs, USA) to confirm the correct insertions and further
383 sequenced with Sanger method (Eurofins Scientific, Luxembourg). *aceE* and *aceF* mutations
384 in the genome of *P. aeruginosa* PAO1 were introduced using the previously developed
385 CRISPR-Cas9 system [55] and following the indicated protocol [56] with the addition of 0.2%

386 arabinose in the growth medium during transformation. To confirm the presence of desired
387 mutations, PCR fragment of the genome around the mutations was amplified and sequenced
388 with Sanger sequencing (Eurofins Scientific, Luxembourg). To perform confocal microscopy
389 analyses, strains were tagged with Gfp using four parental mating using a mini Tn7 delivery-
390 method [57] but with the additional supplementation of 5 mM acetate to ensure growth of
391 PDHc dysregulated target strains. Transformants were identified by green fluorescence and
392 validated by comparing growth rate to the untagged target strain.

393 Bacteria were grown in Synthetic Cystic Fibrosis Media 2 (SCFM2)[58]. To reduce viscosity and
394 allow for HPLC analysis, DNA and mucins were excluded [59]. Cultures were grown at 37 °C and
395 250 rpm.

396

397 *Dynamic exo-metabolomics analyses*

398 Sampling of supernatants was performed in 96-well deep well plates (Cat. No. 0030502302;
399 Eppendorf, Hamburg, Germany) with an air:liquid ratio of 1:1 using a high-throughput
400 dilution-based growth method as previously described [60]. Immediately before sampling, OD_{600}
401 of the cultures were measured in a Synergy™ MX microtiter plate reader (BioTek Instruments
402 Inc., Winooski, VT, USA). Supernatants were stored at -80 °C until HPLC-analysis. For organic
403 acids and sugars (glucose, lactate, formate, acetate and pyruvate), a Dionex Ultimate 3000
404 system (Thermo Scientific,Waltham, United States) with a HPx87H ion exclusion column (125-
405 0140, Aminex, Dublin, Ireland), equipped with a guard column (125-0129, BioRad, Hercules,
406 California, United States) and guard column holder (125-0131, BioRad, Hercules, California,
407 United States) was used. Samples were injected with an injection volume of 20 μL and eluted,
408 using a 5 mM H_2SO_4 mobile phase, at an isocratic flow of 0.6 mL min^{-1} at 45 °C for 30 min.
409 Pyruvate was analysed by UV detection at a wavelength of 210 nm, using a System Gold 166
410 UV-detector (Beckman Coulter, Brea, United States), while the rest of the metabolites were
411 analysed by RI detection, using a Smartline RI detector 2300 (KNAUER Wissenschaftliche
412 Geräte, Berlin, Germany). For amino acids (aspartic acid, glutamic acid, serine, histidine,
413 glycine, threonine, arginine, alanine, tyrosine, valine, phenylalanine, isoleucine, leucine,
414 lysine and proline), 20 μL of the thawed sample was diluted 1:10 by mixing with 80 μL
415 Ultrapure MilliQ water and 100 μL of internal standard (20 μg/mL 2-aminobutyric acid and

416 sarcosine) before injection of 56.5 μL into the instrument. Prior to injection into the column,
417 derivatization of amino acids was performed in the HPLC-instrument by automatic mixing
418 with the following eluents: (i) 0.5% (v/v) 3-mercaptopropionic acid in borate buffer 0.4 M at
419 pH 10.2; (ii) 120 mM iodoacetic acid in 140 mM NaOH; (iii) OPA reagent (10 mg/mL *o*-
420 phtalaldehyde and 3-mercaptopropionic acid in 0.4 M borate buffer); (iv) FMOC reagent (2.5
421 mg/mL 9-fluorenylmethyl chloroformate in acetonitrile); and (v) buffer A (40 mM Na_2HPO_4,
422 0.02% (w/v) NaN_3 at pH = 7). Following derivatization, the samples were separated
423 isocratically on a Dionex Ultimater 3000 HPLC with fluorescence detector (Thermo Scientific,
424 Waltham, United States) through a Gemini C18 column (00F-4439-E0, Phenomenex, Værløse,
425 Denmark) equipped with a SecurityGuard Gemini C18 guard column (AJ0-7597, Phenomenex,
426 Værløse, Denmark) with 5 mM H_2SO_4 at a flowrate of 1 mL min^{-1} at 37 °C for 31 min. Amino
427 acids were detected using an UltiMate™ 3000 Fluorescence variable wavelength UV detector
428 (FLD-3400RS, Waltham, Massachusetts, United States).

429

430 *Proteomic analyses*

431 To maintain a 1:1 air:liquid ratio, as in the metabolomic analysis, 25 mL SCFM cultures were
432 inoculated from ON cultures in 50 mL Falcon tubes at OD_{600} of 0.05 and then incubated in an
433 orbital shaker at 37 °C and 250 rpm until sampling by centrifugation at mid-exponential phase.
434 Five biological replicates were analysed for PAO1 and the clinical isolates while three
435 biological replicates for the PAO1 derivative strains *aceE* and *aceF* both in presence and
436 absence of 5 mM acetate. Pellets were washed twice with PBS and stored at -80C until protein
437 extraction. For experiment with clinical isolates, protein extraction was done in Lysis buffer A
438 (100 mM Tris, 50 mM NaCl, 1 mM tris(2-carboxyethyl)phosphine (TCEP), 10% glycerol, pH =
439 7.5) with *cOmplete Mini protease inhibitor* (Roche) by sonication at amplitude 10 for 3x 10s
440 cycles with 20s cooling between, followed by acetone precipitation and resuspension in Lysis
441 buffer B (6 M Guanidinium hydrochloride, 5 mM TCEP, 10 mM chloroacetamide, 100 mM Tris–
442 HCl, pH = 8.5). For experiment with PAO1 derivative mutant strains, protein extraction was
443 done in Lysis buffer B by bead beating with 3-mm zirconium oxide beads at 99 °C for 5 min. in
444 a Tissuelyzer (Retsch, MM 400) at 25 Hz, then boiled, still at 99 °C, in heat block (Eppendorf
445 Thermomixer C) for 10 min. while shaking/mixing at 2000 rpm. In both cases, protein
446 concentrations were determined by micro BCA™ Protein Assay Kit (Thermo Scientific, prod

447 #23235) and 100 μg protein was used for trypsin digest in Trypsin/Lys-C Buffer (0.1 μg/μL
448 trypsin, 50 mM Ammonium Bicarbonate). The reaction was stopped by addition of 10 μL 10%
449 TFA and samples were desalted by stagetipping with C18 filter plugs (Solaµ HRP 2 mg/1 ml 96
450 well plate, Thermo Scientific). Peptide samples were stored in 40 μL of 0.1% Formic acid at 4
451 °C until LC-MS analysis.

452 For the experiment with clinical isolates, LC-MS/MS was carried out using a CapLC system
453 (Thermo Fisher Scientific Inc., Waltham, USA) coupled to an Orbitrap Q-exactive HF-X mass
454 spectrometer (Thermo Fisher Scientific Inc., Waltham, USA). The first samples were captured
455 at a flow of 10 μL/min on a precolumn (µ-pre-column C18 PepMap 100, 5 μm, 100 Å) and then
456 at a flow of 1.2 μL/min. Peptides were separated on a 15 cm C18 easy spray column (PepMap
457 RSLC C18 2 µm, 100Å, 150 µmx15cm). The applied gradient went from 4% acetonitrile in water
458 to 76% over a total of 60 minutes. MS-level scans were performed with Orbitrap resolution
459 set to 60,000; AGC Target 3.0e6; maximum injection time 50 ms; intensity threshold 5.0e3;
460 dynamic exclusion 25 sec. Data dependent MS2 selection was performed in Top 20 Speed
461 mode with HCD collision energy set to 28% (AGC target 1.0e4, maximum injection time 22 ms,
462 Isolation window 1.2 m/z). For the experiment with the *aceE* and *aceF* mutant strains,
463 peptides were loaded onto a 2 cm C18 trap column (ThermoFisher 164946), connected in-line
464 to a 15cm C18 reverse-phase analytical column (Thermo EasySpray ES904) using 100% Buffer
465 A (0.1% Formic acid in water) at 750bar, using the Thermo EasyLC 1200 HPLC system, and the
466 column oven operating at 30 °C. Peptides were eluted over a 70 minute gradient ranging from
467 10% to 60% of 80% acetonitrile, 0.1% formic acid at 250 nL/min, and the Orbitrap Exploris
468 instrument (Thermo Fisher Scientific) was run in DIA mode with FAIMS Pro™ Interface
469 (ThermoFisher Scientific) with CV of -45 V. Full MS spectra were collected at a resolution of
470 120,000, with an AGC target of 300% or maximum injection time set to 'auto' and a scan range
471 of 400–1000 m/z. The MS2 spectra were obtained in DIA mode in the orbitrap operating at a
472 resolution of 60.000, with an AGC target 1000% or maximum injection time set to 'auto', and
473 a normalised HCD collision energy of 32. The isolation window was set to 6 m/z with a 1 m/z
474 overlap and window placement on. Each DIA experiment covered a range of 200 m/z resulting
475 in three DIA experiments (400-600 m/z, 600-800 m/z and 800-1000 m/z). Between the DIA
476 experiments a full MS scan is performed. MS performance was verified for consistency by

477 running complex cell lysate quality control standards, and chromatography was monitored to
478 check for reproducibility.

479

480 *Phenotypic characterizations*

481 Growth curves were performed by inoculating 1 μL of ON culture in 149 μL of media, using
482 96-well microtiter plates (Cat. No. 650001; Greiner Bio-One, Kremsmünster, Austria), covered
483 with plate seals (Ref. 4306311, Thermo Fisher Scientific, United Kingdom) and incubated at
484 37 °C and 250 rpm in a BioTek ELx808 Absorbance Microtiter Reader (BioTek Instruments Inc.,
485 Winooski, VT, USA) for 24 - 48 hours. Antibiotic MICs were determined by microdilution. ON
486 cultures were standardized to OD_{600} = 0.5 and diluted 1:2500 to reach 5x 10^5 CFU/mL in fresh
487 SCFM2 media (LB for Azithromycin). Growth assays were performed at increasing antibiotic
488 concentrations and MIC determined based on final OD. Resistance to oxidative stress was
489 measured as the diameter of clearance zones around diffusion disks saturated with 5 μL of
490 fresh 30% H_2O_2 after 24 hours incubation at 37 °C on LB agar plates cast with 3 mL overlay
491 agar containing 100 μL of LB ON culture standardized to OD_{600} = 1. Pyoverdine production was
492 measured as the fluorescence at 400/460 nm excitation/emission on a Synergy H1 Hybrid
493 Multi-Mode Reader (BioTek Instruments, Winooski, VT, USA) of supernatants normalized
494 against OD_{600} of ON cultures in King's B medium. Biofilm formation assay was done as
495 previously described for NUNC peg lids [61] (NUNC cat no. 445497). Motility was measured as
496 the diameter of the motility zone around single colonies deposited in middle layer of 0.3%
497 (swimming), surface layer of 0.6% (swarming) or bottom layer of 1.5% (twitching) LB agar
498 motility plates, after incubation at 37 °C for 24 - 48 hours. For PAO1 wt and *aceEF* mutant
499 strains, pyruvate secretion was determined from supernatants of samples taken after 0, 4, 8
500 and 24 hours of growth in SCFM2. Supernatants were stored at -80C and analysed by the HPLC
501 method also used for exo-metabolomics.

502

503 *Infection of ALI cultures*

504 For the Air-Liquid Interface (ALI) infections the BCi-NS1.1 cells were used [62]. Cells were
505 cultured in Pneumacult-Ex Plus medium (STEMCELL Technologies, 05040) supplemented with

506 Pneumacult-Ex 50x supplement (STEMCELL Technologies, 05008), 96 ng/mL hydrocortisone
507 (STEMCELL Technologies, 07925) and 10 μM Y-27632 ROCK inhibitor (Bio-Techne #1254/10)
508 in a 37 °C, 5% CO_2 humidified incubator. Following expansion, 1.5 x 10^5 cells were seeded onto
509 6.5-diameter-size transwells with 0.4 μm pore polyester membrane inserts (Corning
510 Incorporated, 3470) previously coated with human type I collagen (Gibco, A1048301). ALI was
511 established once cells reached full confluency by removing media from the apical chamber
512 and replacing media in the basolateral chamber with Pneumacult-ALI maintenance medium
513 (STEMCELL Technologies, 05001). Pneumacult-ALI maintenance medium was supplemented
514 with Pneumacult-ALI 10x supplement (STEMCELL Technologies, 05003), Pneumacult-ALI
515 maintenance supplement (STEMCELL Technologies, 05006), 480 ng/mL hydrocortisone and 4
516 μg/mL heparin (STEMCELL Technologies, 07980). ALI cultures were grown in a 37 °C, 5% CO_2
517 humidified incubator for 30 days, with media replacement every 2-3 days. Epithelial
518 polarization was monitored by measurements of the transepithelial electrical resistance
519 (TEER) using a chopstick electrode (STX2; World Precision Instruments). Following 15 days
520 under ALI conditions, the apical surface was washed with PBS every media change to remove
521 accumulated mucus. Biological replicates of bacterial strains were obtained from single
522 colonies on LB agar plates grown ON as precultures in LB and then diluted to an OD_{600} of 0.05
523 before sampling at mid-exponential phase by centrifugation, washing with PBS and
524 resuspending in PBS at a density of 10^5 CFU/mL. Fully-differentiated BCi-NS1.1 cells were
525 inoculated with 10^3 CFU from the apical side, diluted in 10 μL PBS. Control wells were
526 incubated with bacteria-free PBS. Cells were incubated for 14 hours at 37 °C, followed by
527 addition of 200 μL PBS to the apical side and measurement of the TEER. CFUs were
528 determined by platting 10 μL of 6-fold serial dilutions on LB-agar plates in technical triplicates
529 both for the initial inoculum, as well as for the apical and basolateral solutions following TEER-
530 measurements. The basolateral media was also used for measurements of LDH and IL-8
531 release in technical triplicates, using the Invitrogen™ CyQUANT™ LDH Cytotoxicity Assay Kit
532 (Invitrogen, C20301) and Human IL-8/CXCL8 DuoSet ELISA Kit (R&D Systems, DY208)
533 according to the manufacturer´s instructions. BCi-NS1.1 cells on transwell inserts were rinsed
534 once with PBS and fixed by adding 4% (wt/vol) paraformaldehyde (PFA) to both apical and
535 basolateral chambers for 20 min at 4 °C. After washing, cells were permeabilized and blocked
536 for 1 hour with a buffer containing 3% BSA, 1% Saponin and 1% Triton X-100 in PBS. Cells were
537 stained on the apical side with Phalloidin-AF488 (Invitrogen, 65-0863-14) and TO-PRO3

538 (Biolegend, 304008) diluted in a staining buffer (3% BSA and 1% Saponin in PBS) at a 1:500
539 dilution for 2 hours at room temperature. Transwells were removed from their supports with
540 a scalpel and mounted on glass slides with VECTASHIELD® Antifade Mounting Medium (VWR,
541 VECTH-1000). Images were acquired with a Carl Zeiss LSM 510 Confocal Laser Scanning
542 Microscope (40× magnification, 1.3 oil) and analysed using the ImageJ software.

543

544 *Data analysis*

545 For genetic analysis, phylogenetic bootstrap consensus tree was constructed by maximum
546 parsimony analysis using the subtree-pruning-regrafting algorithm and a bootstrap consensus
547 value of 50% using the software MEGAX [63]. The tree was inferred from concatenated strings
548 of 8600 positions in the genome containing non-intergenic SNPs relative to PAO1. Enrichment
549 analyses of functional categories was done using the DAVID Functional Annotation
550 Bioinformatics Microarray Analysis tool from lists of mutated Locus Tags in each infection
551 lineage with the reference genome set as *Pseudomonas aeruginosa*. Genomic data are
552 enclosed in Supplementary Data 1.

553 For exometabolomics, all chromatograms were analysed and used to construct standard
554 curves constructed for absolute quantification of concentrations for all 20 metabolites, using
555 software Chromeleon v7.2.9. All other analysis of exo-metabolomic data was done in JMP Pro
556 15.0. To compare between different strains and media batch-effects, OD_{600} was normalized
557 against final OD_{600} of that strain in the experiment and concentrations were normalized
558 against specific concentrations in SCFM2 controls for each batch. Missing values were
559 replaced with 20% of lowest value detected for any metabolite in any sample. Principal
560 component analysis (PCA) and hierarchical cluster analysis (HCA) were done on $C_{metabolite}$ of all
561 quantified metabolites for 16 samples (8 time-points from biological duplicates) of each
562 strain. PCA was done on covariance and HCA using Ward's method for cluster analysis.
563 Metabolite half-life (OD_{50}), defined as the normalized OD_{600}-value, where 50% of the starting
564 concentration of a metabolite is present, was calculated from the sigmoidal mechanistic
565 growth model (Equation: a(1 – bExp(–cx)) where a = asymptote, b = scale and c = rate).
566 Metabolomics data are enclosed in Supplementary Data 2.

567 For the experiment with clinical isolates, proteomic raw files were analysed using Proteome
568 discoverer 2.4 software with the following settings: Fixed modifications: Carbamidomethyl (C)
569 and Variable modifications: oxidation of methionine residues. First search mass tolerance 20
570 ppm and a MS/MS tolerance of 20 ppm. Trypsin as enzyme and allowing one missed cleavage.
571 FDR was set at 0.1%. The Match between runs window was set to 0.7 min. Quantification was
572 only based on unique peptides and normalization between samples was based on total
573 peptide amount. For the experiment with mutant strains, raw files were analyzed using
574 Spectronaut™ (version 16.2). Dynamic modifications were set as Oxidation (M) and Acetyl on
575 protein N-termini. Cysteine carbamidomethyl was set as a static modification. All results were
576 filtered to a 1% FDR, and protein quantitation done on the MS1 level. The data was
577 normalized by RT dependent local regression model [64] and protein groups were inferred by
578 IDPicker. In both cases, spectra were matched against the *Pseudomonas aeruginosa* PAO1
579 reference proteome (UniProt Proteome ID UP000002438). In both experiments, any protein
580 that was not quantified in at least 3 of 5 or 2 of 3 biological replicates for all strains were
581 excluded from the analysis. Using JMP Pro 15.0, abundances were normalized by Log_2-
582 transformation and biological replicates used for missing value imputation. PCA Wide was
583 done on correlations and HCA was done using Ward's method for mean Log_2(abundance) and
584 Log_2(Fold change) was calculated for relevant comparisons. Differential expression was
585 determined by two-way ANOVA with Tukey's multiple comparisons test, using GraphPad
586 Prism 9.3.1, and defined as those protein-comparisons where Adjusted *P* value ≤ 0.05 and
587 Log_2(Fold Change) ≥ |0.6|. Enrichment analysis was done as in the genetic analysis, but with
588 input lists containing Locus Tags of proteins that were differentially expressed, separated into
589 lists of upregulated and downregulated proteins respectively, for each of the relevant strain-
590 comparisons. Proteomics data are enclosed in Supplementary data 3 and 4.

591 Growth rates and maxOD were calculated in JMP Pro 15.0. Blanks were first subtracted from
592 OD_{600}-measurements and values converted to cm^{-1} (using Greiner dimensions for pathlength).
593 The stationary phase was excluded, and growth rates were calculated by fitting the
594 Exponential 3P model to the exponential phase ($r^2 > 0.99$). Mean ± sd was calculated from
595 biological replicates. GraphPad Prism 9.3.1 was used for statistical analysis of biofilm
596 formation, motility, redox sensitivity, pyoverdine production and MICs (See Figure S5 for
597 details), as well as for ALI infection experiments. ALI data are represented as mean ± SEM.

598 Replicates represent independent experiments performed with cells from different passages.
599 Statistical comparisons were calculated using Two-Way ANOVA for TEER and CFU
600 measurements and One-Way ANOVA for LDH and IL-8 measurements. Statistical significance
601 was considered for p-value < 0.05. All figures were finalized in Adobe Illustrator Artwork 27.0.

602

603 *Data availability*

604 The authors declare that all data necessary for supporting the findings of this study are
605 enclosed in this paper (Supplementary Data 1-4). All genomic data is publicly available
606 through the SRA database and has been published previously by Marvig et al., (2015) [19].

607

608 **Acknowledgements**

609 The work was supported by The Novo Nordisk Foundation (grant numbers NNF20CC0035580
610 and NNF19OC0056411), the UK CF Trust (grant number SRC017) and the Independent
611 Research Fund Denmark/Natural Sciences (grant number 9040- 00106B). The Basal Cell
612 Immortalized Non-Smoker 1.1 (BCi-NS1.1) cell line was a kind gift from Professor Ronald G.
613 Cristal (Weil Cornell Medical College, New York, USA).

614

615 **Author contributions**

616 BHP, SM and RLR designed the project. BHP, FBS and IP performed the experiments and
617 verified the data. HKJ provided the strains and the clinical data. MW enabled the proteomic
618 analyses. BHP and RLR wrote the first draft of the paper, which after review by all authors,
619 was revised according to the co-authors' suggestions. All authors approved the final version
620 of the manuscript.

621

622 **Competing interests**

623 The authors declare no competing interests.

624

625 **Figures and figure legends**

626

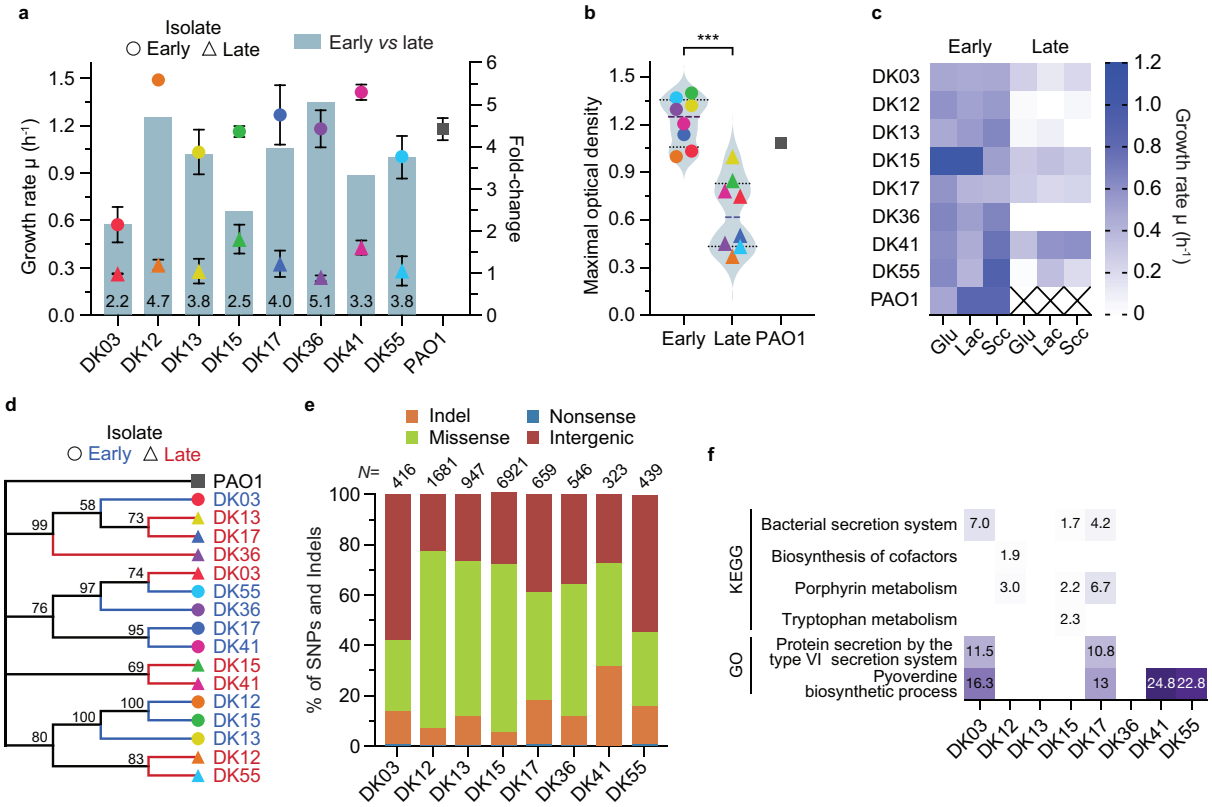

627

628 Figure 1: Collection of *Pseudomonas aeruginosa* clinical strains. a) Growth rate (hour^{-1}) of
629 early (circles), late (triangles) and PAO1 (square) strains coloured by their clone type. The fold
630 change of growth rate from early to late is shown as bar chart on the right y axis and as
631 number value at the base of each bar. b) The maximal optical density (maxOD) of all isolates,
632 grouped by early *vs* late comparison. Statistical significance was calculated by Unpaired Welch
633 t-test and indicated as *** ($p < 0.001$). c) Growth rate (hour^{-1}) of each strain in M9 minimal
634 media containing 20 mM of a single carbon source glucose (Glu), lactate (Lac) or succinate
635 (Suc). d) Maximum parsimony reconstruction of the analysed strains. The tree is based on
636 8600 missense and nonsense SNP mutations accumulated during within patient evolution.
637 Branches corresponding to partitions reproduced in less than 50% of bootstrap replicates are
638 collapsed. The percentages of replicate trees in which the associated taxa clustered together
639 in the bootstrap test (500 replicates) are shown next to the branches. e) Distribution of
640 mutations identified in the genome of each infection lineage. Total number of mutations
641 (accumulated or reverted) in the specific lineage is indicated above each bar. f) Enrichment

642 analysis on mutated genes for KEGG and GO categories. The fold-enrichment is indicated for
643 each category.

644

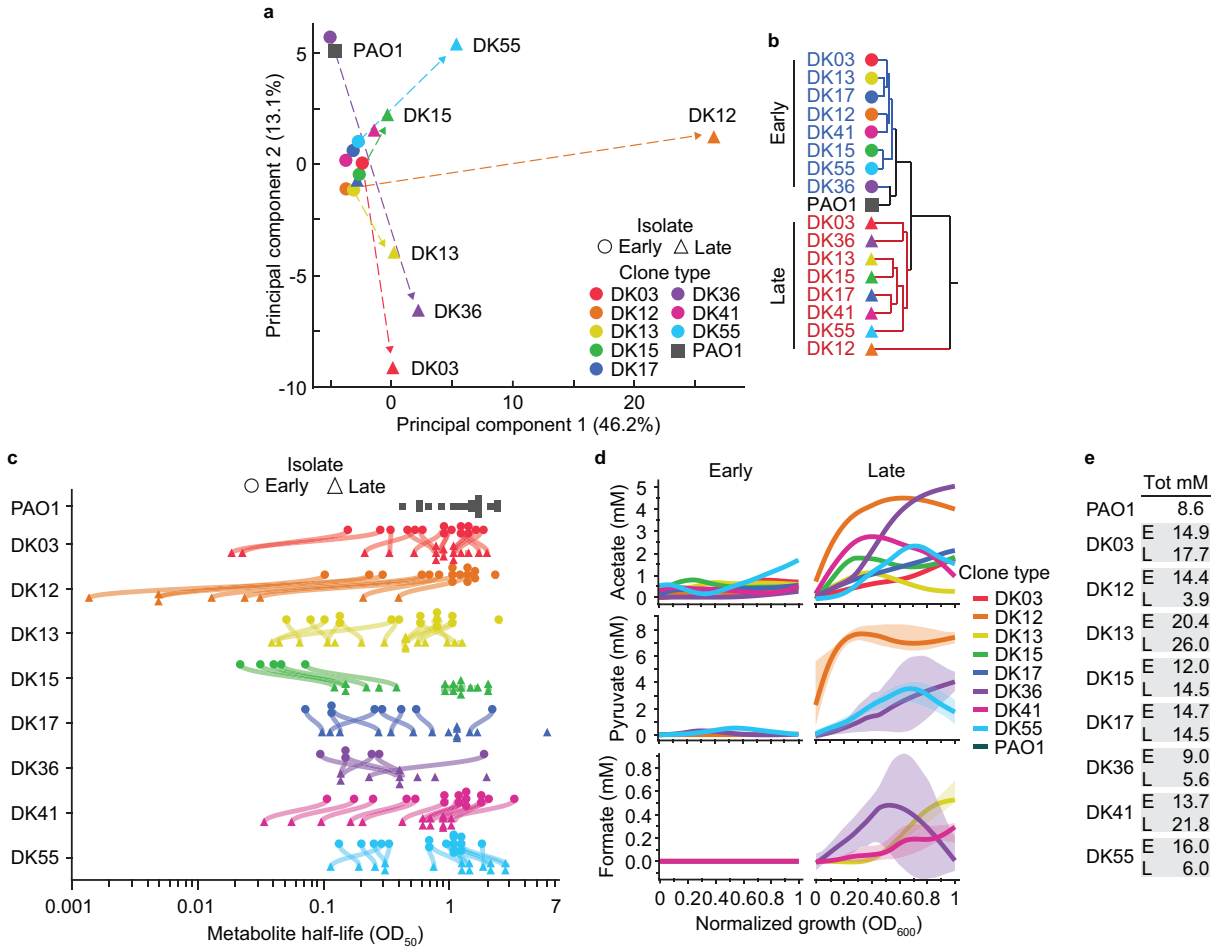

645

646 Figure 2: Exo-metabolomics analysis reveals adapted metabotypes. a) PCA showing
647 separation of strains based on their time-resolved exo-metabolomes. Strains are shown as
648 circles (early), triangles (late) and square (PAO1), with dashed arrows indicating most notable
649 trajectories from early to late, coloured by clone type. b) HCA of exo-metabolomics data,
650 showing a general separation between early and late strains. Branches for early isolates are
651 indicated in blue, late isolates in red and PAO1 in black. c) Assimilation hierarchies of the
652 analysed metabolites. Each symbol represents the half-life (OD_{50}) of a specific metabolite
653 while each line connects the same metabolite for each pair of early and late isolates. d)
654 Secretion plots showing variations in concentration of acetate, pyruvate and formate (mM)
655 relative to the normalized growth (OD_{600}). Shaded areas indicate the 95% confidence
656 intervals. e) Table showing the total amount (mM) of carbon sources assimilated for each

strain. Clone types are separated by grey boxes with “E” indicating early and “L” indicating late isolate.

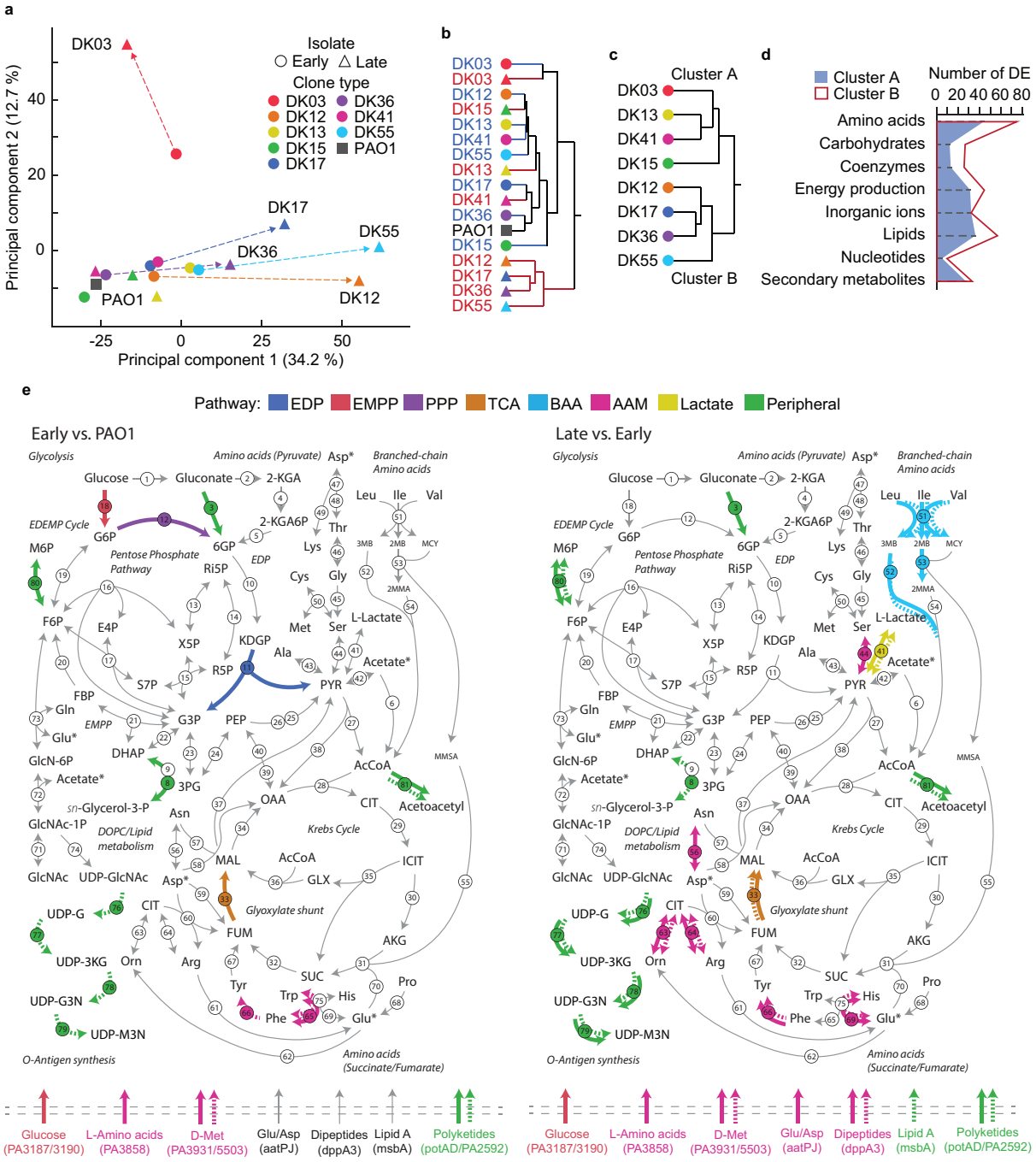

Figure 3: Proteome composition changes support metabolism specialization. a) PCA showing separation of strains based on their mid-exponential proteomes. Strains are shown as circles (early), triangles (late) and square (PAO1), with dashed arrows indicating most notable trajectories from early to late, coloured by clone type. b) HCA of proteomics data, showing a

general separation between early and late strains. Branches for early isolates are indicated in blue, late isolates in red and PAO1 in black. c) HCA of differentially expressed proteins within the COG categories related to metabolism. d) Parallel plots of the number of differentially expressed (DE) proteins within the COG categories related to metabolism in cluster A (Blue, shaded) and B (red, transparent). e) Metabolic maps showing the differences between early clinical strains *vs* PAO1 (left) and late *vs* early clinical strains (right) in pathways related to the catabolism of nutrients present in SCFM through central carbon metabolism. Arrows represent individual metabolite-conversions coloured by their pathway. Reactions are coloured if the underlining enzyme is differentially expressed in more than one clone type – either with dashed (downregulated) or full (upregulated) lines, or both. Enzymes responsible for each reaction are indicated by numbered circles. For details on individual enzymes, see Figure S2. Transporters are shown at the bottom as arrows crossing bacterial cell membrane with their specific transported metabolites. Asp, Glu and acetate are labelled with * to indicate that they are represented in two places on the map, due to their involvement in different parts of central carbon metabolism.

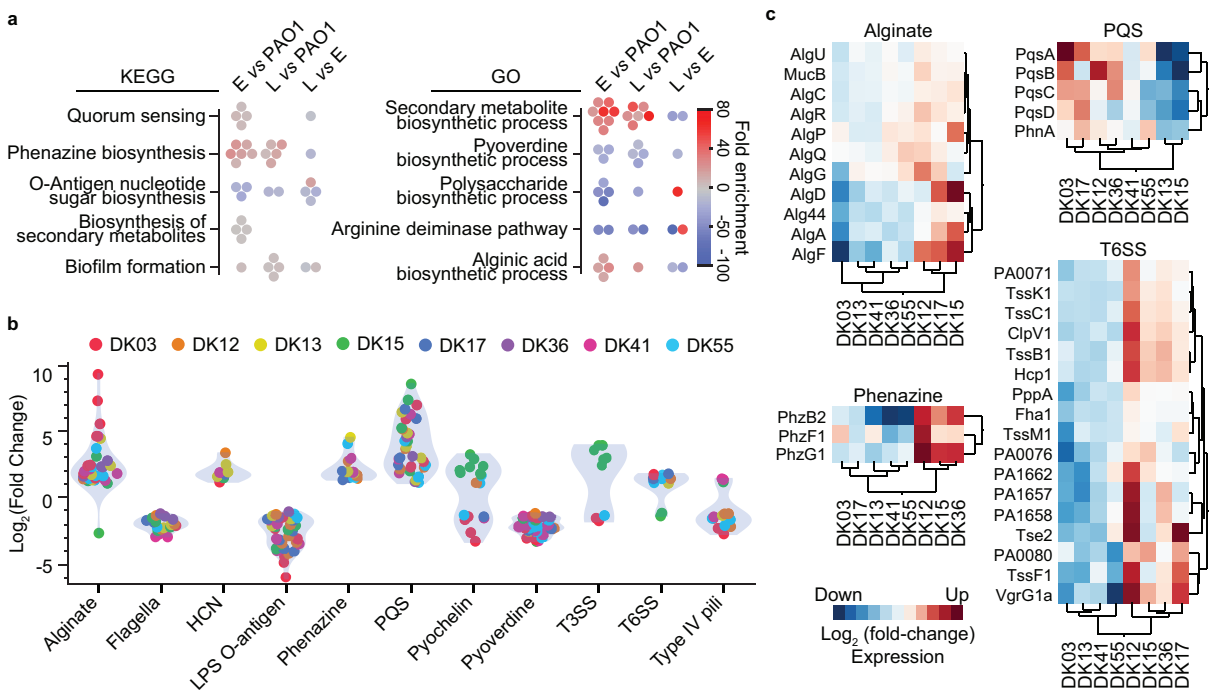

Figure 4: Expression of virulence factors differs in clinical strains *vs* PAO1. a) Enrichment analysis for KEGG and GO terms by the specific comparisons (Early *vs* PAO1; Late *vs* PAO1;

684 Late *vs* Early). Icons represent individual lineages and are coloured by fold-enrichment. b)
685 Differential expression of virulence factors in early clinical strains *vs* PAO1. Only differentially
686 expressed proteins are represented and are coloured by clone type. c) HCA of differentially
687 expressed proteins of virulence factors in late *vs* early clinical strains.

688

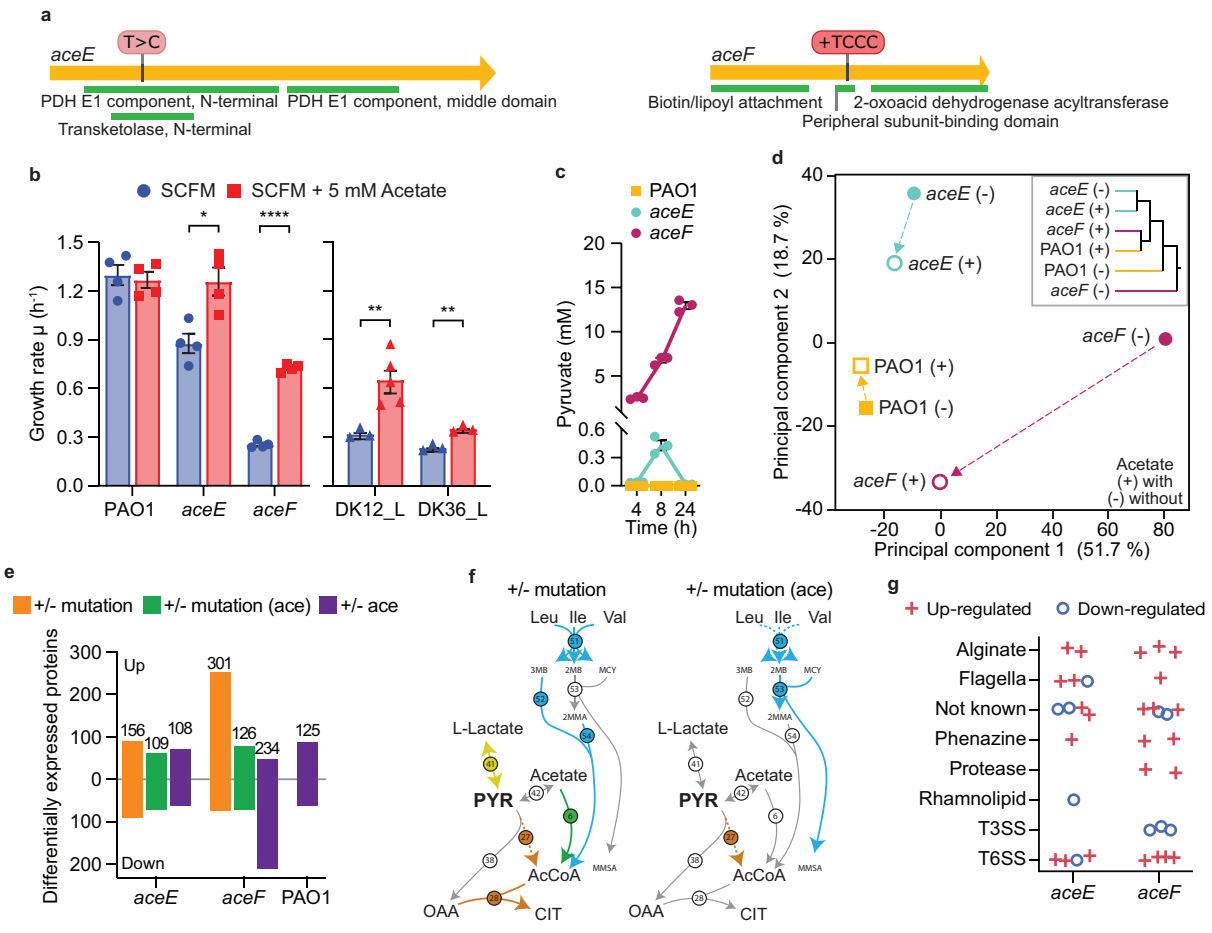

689

690 Figure 5: *aceE* and *aceF* mutations cause metabolic specialization. a) Schematic of the *aceE*
691 and *aceF* genes including location and type of mutation found in the DK36 (*aceE*) and DK12
692 (*aceF*) late strains. b) Growth rate (hour^{-1}) in SCFM2 (blue) and SCFM2 supplemented with 5
693 mM acetate (red) for PAO1, *aceE* and *aceF* mutant strains, and DK12 and DK36 late clinical
694 isolates. Bars indicate mean ± SEM, with icons representing biological replicates. Statistical
695 significance is assessed by two-tailed unpaired parametric Welch t-test and indicated as * (p
696 < 0.05), ** (p < 0.01) or **** (p < 0.0001). c) Pyruvate secretion (mM) for PAO1 wt (yellow),
697 *aceE* (cyan) and *aceF* (magenta) mutant strains over 24 hours. Icons represent biological
698 replicates. d) PCA and HCA of whole-cell proteomics for PAO1 wt and *aceE* and *aceF* mutant

699 strains. Filled icons indicate without (-) and unfilled icons indicate with (+) 5 mM acetate. e)
700 Number of differentially expressed proteins in presence *vs* absence of acetate (purple), for
701 mutant strain *vs* PAO1, either in absence (orange) or presence (green) of acetate. f) Metabolic
702 map of enzymes related to pyruvate and acetyl-CoA metabolism for mutant strains *vs* PAO1
703 in absence (left) or presence (right) of acetate. Reactions are coloured by their pathway if the
704 underlining enzyme is differentially expressed (dashed if downregulated or continuous if
705 upregulated). Enzymes responsible for each reaction are indicated by numbered circles. For
706 details on individual enzymes, see Figure S6. g) Differentially expressed proteins involved in
707 virulence in *aceE* and *aceF* mutant strains *vs* PAO1 in absence of acetate. Icons indicate
708 specific proteins that are upregulated (red plus) or downregulated (blue circle).

709

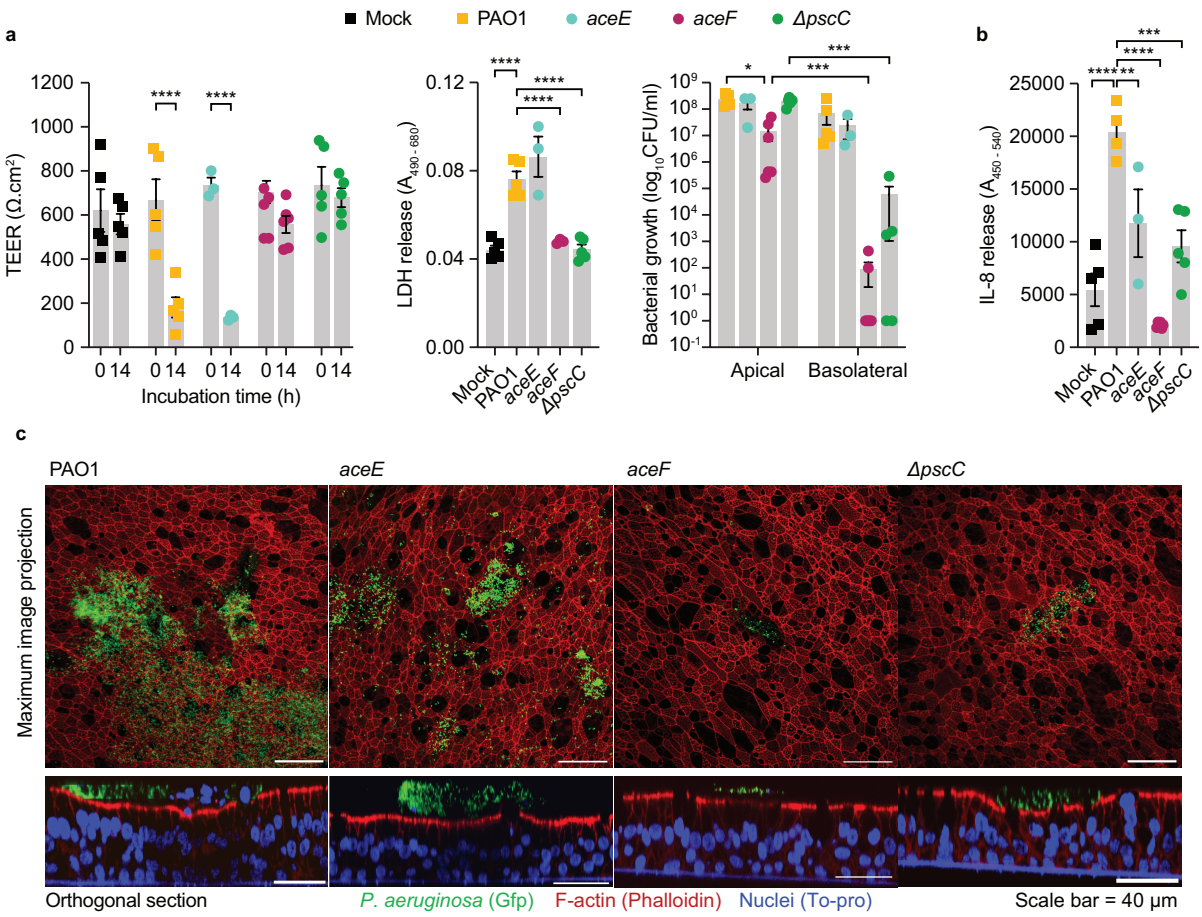

710

711 Figure 6**:** Aggressiveness of *aceE* and *aceF* strains in Air-Liquid Interface airway infections. a)
712 Mean ± SEM of Transepithelial Electrical Resistance (TEER) ($\Omega \cdot cm^2$), LDH release and Colony
713 Forming Units (CFU) in the apical and basolateral ALI compartments after 14 hours of infection
714 in fully differentiated BCi-NS1.1 cells. b) IL-8 release into the basolateral media indicating

715 immunogenicity caused by the invading bacteria. Icons represent each biological replicates.
716 Mock represents un-infected control cells. Statistical significance was determined by Two-
717 Way ANOVA for TEER and CFU measurements and One-Way ANOVA for LDH and IL-8
718 measurements and indicated as * ($p < 0.05$), ** ($p < 0.01$), *** ($p < 0.001$) and **** ($p <$
719 0.0001). c) Confocal images of ALI transwells following infection with *P. aeruginosa* in green
720 (Gfp), epithelium in red (Phalloidin) and nuclei in blue (To-pro). Scale bar = 40 μm.

721

722 Figure S1: a) Number of differentially expressed proteins (top) and Log_2(Fold change) of
723 individual differentially expressed proteins in late vs. early clinical isolates, separated by
724 lineage and on the x-axis by COG categories. b) Complete enrichment analysis showing fold-
725 enrichments separated by comparison and lineage on x-axis and by KEGG and GO terms on y-
726 axis.

727

728 Figure S2: a) Metabolic map in the same style as Fig. 3E for late clinical strains vs PAO1. b)
729 Table of genes/Locus Tags of all metabolic enzymes included in the map. c-d) Bar charts
730 showing Log_2(Fold change) of all differentially expressed proteins highlighted on the
731 metabolic maps. Icons coloured by lineage and separated into three comparisons on x-axis
732 (Early vs PAO1; Late vs Early; Late vs PAO1). Panel c contains metabolic enzymes and panel d
733 contains transporters.

734

735 Figure S3: a) Hierarchical cluster analysis in the same style as Fig. 4C, showing differential
736 expression in late vs early clinical strains for several more virulence categories. b) The
737 Log_2(Fold change) of differentially expressed proteins in late vs early clinical strains separated
738 into the relevant virulence categories and further separated into the two main clusters from
739 panel a. Icons are coloured by lineage and lines depict the difference in mean Log_2(Fold
740 change) between the two clusters.

741

742 Figure S4: Schematic of all 18 unique mutations observed for *aceE* (top) and *aceF* (bottom) in
743 our collection of clinical isolates of *P. aeruginosa*. Grey lines indicate mutation site and letters
744 indicate nucleotide-sequence coloured by type of mutation.

745

746 Figure S5: a) Potential for biofilm formation (surface attachment) of PAO1 wt (blue), as well
747 as *aceE* (red) and *aceF* (green) mutant strains and DK12 & DK36 late clinical strains after 24
748 and 48 hours respectively. For the clinical isolates, strain is indicated on the x-axes and
749 incubation time is indicated as blue (24 hours) and red (48 hours). Attachment is measured
750 as the ratio of surface-attached cells (OD_{590}) to total number of cells (OD_{600}) after incubation.
751 For PAO1 wt and *aceE* and *aceF* mutants, all strains were compared by One-Way ANOVA. For
752 clinical isolates, each strain was compared to itself after 24 and 48 hours of incubation
753 respectively, using two-tailed unpaired parametric Welch t-test. Significance is indicated as
754 'ns' ($p > 0.05$), * ($p < 0.05$), ** ($p < 0.01$), *** ($p < 0.001$). Same colouring and statistical analysis
755 for PAO1 and mutant strains in panel b-d. b) Motility measured as the diameter (mm) of the
756 zone of growth in motility plates (LB agar). Swimming motility was clearly visible after 24
757 hours of incubation. Swarming and twitching plates required 48 hours of incubation. c) Redox
758 sensitivity measured as the diameter of the clearance zone (mm) on bacterial lawns (LB agar)
759 of each strain from H_2O_2 diffusion disks after 24 hours. d) Pyoverdine production measured
760 as relative fluorescence (F/OD_{600}) of each strain after 24 hours of growth in King's B medium.
761 For panel a-d, icons indicate biological replicates and bars represent the mean ± SEM. e) MICs
762 of PAO1 wt and *aceE* and *aceF* mutant strains. Each cell represents the maxOD of growth
763 curves under the given condition, following the colour gradient to the right of each heatmap.
764 The MIC is the concentration where no growth is observed (white). Each heat map shows the
765 MIC for all three strains for a given antibiotic (Ceftazidime, Meropenem, Piperacillin,
766 Azithromycin, Chloramphenicol, Ciprofloxacin and Tobramycin). Concentrations (μg/mL)
767 increase 2-fold downward on the vertical axis and the specific strain is given on the horizontal
768 axis. Azithromycin MICs were determined in LB, while all other MICs were determined in
769 SCFM2. Piperacillin was used in combination with the β-lactamase inhibitor Tazobactam.

770

771 Figure S6: a) Metabolic map in the same style as Fig. 3E for *aceF* mutant strain vs PAO1
772 reference in SCFM2 in absence (left) and presence (right) of acetate. b) Parallel plot showing
773 the number of differentially expressed proteins, separated by metabolic COG categories, in
774 *aceE* (cyan) and *aceF* (magenta) mutant strains vs PAO1. c) Enrichment analysis showing fold
775 enrichment on x-axis separated by KEGG and GO terms on y-axis for *aceE* (left) and *aceF* (right)
776 mutant strains vs PAO1.

777

778 Figure S7: Longitudinal collection of *P. aeruginosa* clinical isolates from CF airways. Icons
779 indicate isolates carrying mutations in genes encoding PDHc (red squares) and/or T3SS
780 (purple triangles) proteins, as well as isolates with no mutations in either (grey dots). Isolates
781 are separated by Clone Type and further separated by patient-specific lineages within Clone
782 Types (A, B, C). The x-axis shows the length of infection (years) since the first isolate of the
783 given lineage.

784 References

785 1. Brown, S.A., Palmer, K.L., and Whiteley, M. (2008). Revisiting the host as a growth medium.
786 Nat Rev Microbiol *6*, 657–666. 10.1038/nrmicro1955.

787 2. Diaz, M.R., King, J.M., and Yahr, T.L. (2011). Intrinsic and extrinsic regulation of type III
788 secretion gene expression in Pseudomonas aeruginosa. Front Microbiol *2*, 1–10.
789 10.3389/fmicb.2011.00089.

790 3. Li, L., Meng, H., Gu, D., Li, Y., and Jia, M. (2019). Molecular mechanisms of Vibrio
791 parahaemolyticus pathogenesis. Microbiol Res *222*, 43–51. 10.1016/j.micres.2019.03.003.

792 4. Malik-Kale, P., Jolly, C.E., Lathrop, S., Winfree, S., Luterbach, C., and Steele-Mortimer, O.
793 (2011). Salmonella- at home in the host cell. Front Microbiol *2*, 1–9.
794 10.3389/fmicb.2011.00125.

795 5. Flannagan, R.S., Cosío, G., and Grinstein, S. (2009). Antimicrobial mechanisms of phagocytes
796 and bacterial evasion strategies. Nat Rev Microbiol *7*, 355–366. 10.1038/nrmicro2128.

797 6. Malhotra, S., Hayes, D., and Wozniak, D.J. (2019). Mucoid Pseudomonas aeruginosa and
798 regional inflammation in the cystic fibrosis lung. Journal of Cystic Fibrosis *18*, 796–803.
799 10.1016/j.jcf.2019.04.009.

800 7. Govan, J.R., and Deretic, V. (1996). Microbial pathogenesis in cystic fibrosis: mucoid
801 Pseudomonas aeruginosa and Burkholderia cepacia. Microbiol Rev *60*, 539–574.
802 10.1111/j.1365-2672.2007.03706.x.

803 8. Henry, R.L., Mellis, C.M., and Petrovic, L. (1992). Mucoid Pseudomonas aeruginosa is a
804 marker of poor survival in cystic fibrosis. Pediatr Pulmonol *12*, 158–161.
805 10.1002/ppul.1950120306.

806 9. Heim, C.E., Bosch, M.E., Yamada, K.J., Aldrich, A.L., Chaudhari, S.S., Klinkebiel, D., Gries, C.M.,
807 Alqarzaee, A.A., Li, Y., Thomas, V.C., et al. (2020). Lactate production by Staphylococcus
808 aureus biofilm inhibits HDAC11 to reprogramme the host immune response during persistent
809 infection. Nat Microbiol *5*, 1271–1284. 10.1038/s41564-020-0756-3.

810 10. Tomlinson, K.L., Lung, T.W.F., Dach, F., Annavajhala, M.K., Gabryszewski, S.J., Groves, R.A.,
811 Drikic, M., Francoeur, N.J., Sridhar, S.H., Smith, M.L., et al. (2021). Staphylococcus aureus
812 induces an itaconate-dominated immunometabolic response that drives biofilm formation.
813 Nat Commun *12*, 1–13. 10.1038/s41467-021-21718-y.

814 11. Riquelme, S.A., Liimatta, K., Wong Fok Lung, T., Fields, B., Ahn, D., Chen, D., Lozano, C., Sáenz,
815 Y., Uhlemann, A.C., Kahl, B.C., et al. (2020). Pseudomonas aeruginosa Utilizes Host-Derived
816 Itaconate to Redirect Its Metabolism to Promote Biofilm Formation. Cell Metab *31*, 1091-
817 1106.e6. 10.1016/j.cmet.2020.04.017.

818 12. La Rosa, R., Johansen, H.K., and Molin, S. (2018). Convergent Metabolic Specialization
819 through Distinct Evolutionary Paths in Pseudomonas aeruginosa. mBio *9*, e00269-18.
820 10.1128/mBio.00269-18.

821 13. Behrends, V., Bell, T.J., Liebeke, M., Cordes-Blauert, A., Ashraf, S.N., Nair, C., Zlosnik, J.E.A.,
822 Williams, H.D., and Bundy, J.G. (2013). Metabolite Profiling to Characterize Disease-related
823 Bacteria. Journal of Biological Chemistry *288*, 15098–15109. 10.1074/jbc.M112.442814.

824 14. La Rosa, R., Johansen, H.K., and Molin, S. (2019). Adapting to the Airways: Metabolic
825 Requirements of Pseudomonas aeruginosa during the Infection of Cystic Fibrosis Patients.
826 Metabolites *9*, 234. 10.3390/metabo9100234.

827 15. Palmer, K.L., Aye, L.M., and Whiteley, M. (2007). Nutritional Cues Control Pseudomonas
828 aeruginosa Multicellular Behavior in Cystic Fibrosis Sputum. J Bacteriol *189*, 8079–8087.
829 10.1128/JB.01138-07.

830 16. La Rosa, R., Johansen, H.K., and Molin, S. (2022). Persistent Bacterial Infections, Antibiotic
831 Treatment Failure, and Microbial Adaptive Evolution. Antibiotics *11*, 419.
832 10.3390/antibiotics11030419.

833 17. Haney, E.F., and Hancock, R.E.W. (2022). Addressing Antibiotic Failure—Beyond Genetically
834 Encoded Antimicrobial Resistance. Frontiers in Drug Discovery *2*, 1–7.
835 10.3389/fddsv.2022.892975.

836 18. Rossi, E., La Rosa, R., Bartell, J.A., Marvig, R.L., Haagensen, J.A.J., Sommer, L.M., Molin, S., and
837 Johansen, H.K. (2021). Pseudomonas aeruginosa adaptation and evolution in patients with
838 cystic fibrosis. Nat Rev Microbiol *19*, 331–342. 10.1038/s41579-020-00477-5.

839 19. Marvig, R.L., Sommer, L.M., Molin, S., and Johansen, H.K. (2015). Convergent evolution and
840 adaptation of Pseudomonas aeruginosa within patients with cystic fibrosis. Nat Genet *47*, 57–
841 64. 10.1038/ng.3148.

842 20. Yang, L., Jelsbak, L., Marvig, R.L., Damkiaer, S., Workman, C.T., Rau, M.H., Hansen, S.K.,
843 Folkesson, A., Johansen, H.K., Ciofu, O., et al. (2011). Evolutionary dynamics of bacteria in a
844 human host environment. Proceedings of the National Academy of Sciences *108*, 7481–7486.
845 10.1073/pnas.1018249108.

846 21. La Rosa, R., Rossi, E., Feist, A.M., Johansen, H.K., and Molin, S. (2021). Compensatory
847 evolution of Pseudomonas aeruginosa's slow growth phenotype suggests mechanisms of
848 adaptation in cystic fibrosis. Nat Commun *12*, 3186. 10.1038/s41467-021-23451-y.

849 22. Lopatkin, A.J., Bening, S.C., Manson, A.L., Stokes, J.M., Kohanski, M.A., Badran, A.H., Earl,
850 A.M., Cheney, N.J., Yang, J.H., and Collins, J.J. (2021). Clinically relevant mutations in core
851 metabolic genes confer antibiotic resistance. Science (1979) *371*, eaba0862.
852 10.1126/science.aba0862.

853 23. Martínez, J.L., and Rojo, F. (2011). Metabolic regulation of antibiotic resistance. FEMS
854 Microbiol Rev *35*, 768–789. 10.1111/j.1574-6976.2011.00282.x.

855 24. Chung, J.C.S., Rzhepishevska, O., Ramstedt, M., and Welch, M. (2013). Type III secretion
856 system expression in oxygen-limited Pseudomonas aeruginosa cultures is stimulated by
857 isocitrate lyase activity. Open Biol *3*. 10.1098/rsob.120131.

858 25. Linares, J.F., López, J.A., Camafeita, E., Albar, J.P., Rojo, F., and Martínez, J.L. (2005).
859 Overexpression of the multidrug efflux pumps MexCD-OprJ and MexEF-OprN is associated
860 with a reduction of type III secretion in Pseudomonas aeruginosa. J Bacteriol *187*, 1384–1391.
861 10.1128/JB.187.4.1384-1391.2005.

862 26. Dacheux, D., Epaulard, O., De Groot, A., Guery, B., Leberre, R., Attree, I., Polack, B., and
863 Toussaint, B. (2002). Activation of the Pseudomonas aeruginosa type III secretion system

requires an intact pyruvate dehydrogenase aceAB operon. Infect Immun *70*, 3973–3977. 10.1128/IAI.70.7.3973-3977.2002.

27. Kao, K.K., and Fink, M.P. (2010). The biochemical basis for the anti-inflammatory and cytoprotective actions of ethyl pyruvate and related compounds. Biochem Pharmacol *80*, 151–159. 10.1016/j.bcp.2010.03.007.

28. O'Donnell-Tormey, J., Nathan, C.F., Lanks, K., DeBoer, C.J., and de la Harpe, J. (1987). Secretion of pyruvate. An antioxidant defense of mammalian cells. Journal of Experimental Medicine *165*, 500–514. 10.1084/jem.165.2.500.

29. Li, J., Diao, B., Guo, S., Huang, X., Yang, C., Feng, Z., Yan, W., Ning, Q., Zheng, L., Chen, Y., et al. (2017). VSIG4 inhibits proinflammatory macrophage activation by reprogramming mitochondrial pyruvate metabolism. Nat Commun *8*, 1–13. 10.1038/s41467-017-01327-4.

30. Price-Whelan, A., Dietrich, L.E.P., and Newman, D.K. (2007). Pyocyanin Alters Redox Homeostasis and Carbon Flux through Central Metabolic Pathways in Pseudomonas aeruginosa PA14. J Bacteriol *189*, 6372–6381. 10.1128/JB.00505-07.

31. Schiessl, K.T., Hu, F., Jo, J., Nazia, S.Z., Wang, B., Price-Whelan, A., Min, W., and Dietrich, L.E.P. (2019). Phenazine production promotes antibiotic tolerance and metabolic heterogeneity in Pseudomonas aeruginosa biofilms. Nat Commun *10*, 1–10. 10.1038/s41467-019-08733-w.

32. Hauser, A.R. (2009). The type III secretion system of Pseudomonas aeruginosa: Infection by injection. Nat Rev Microbiol *7*, 654–665. 10.1038/nrmicro2199.

33. Horna, G., and Ruiz, J. (2021). Type 3 secretion system of Pseudomonas aeruginosa. Microbiol Res *246*, 126719. 10.1016/j.micres.2021.126719.

34. Rossi, E., Falcone, M., Molin, S., and Johansen, H.K. (2018). High-resolution in situ transcriptomics of Pseudomonas aeruginosa unveils genotype independent patho-phenotypes in cystic fibrosis lungs. Nat Commun *9*, 3459. 10.1038/s41467-018-05944-5.

35. Yang, R., Zhu, S., and Tonnessen, T.I. (2016). Ethyl pyruvate is a novel anti-inflammatory agent to treat multiple inflammatory organ injuries. Journal of Inflammation (United Kingdom) *13*, 1–11. 10.1186/s12950-016-0144-1.

36. Li, H., Xia, Y., Tian, Z., Jin, Y., Bai, F., Cheng, Z., Swietnicki, W., Wu, W., and Pan, X. (2022). Dihydrolipoamide Acetyltransferase AceF Influences the Type III Secretion System and Resistance to Oxidative Stresses through RsmY/Z in Pseudomonas aeruginosa. Microorganisms *10*. 10.3390/MICROORGANISMS10030666.

37. Dacheux, D., Epaulard, O., de Groot, A., Guery, B., Leberre, R., Attree, I., Polack, B., and Toussaint, B. (2002). Activation of the Pseudomonas aeruginosa type III secretion system requires an intact pyruvate dehydrogenase aceAB operon. Infect Immun *70*, 3973–3977. 10.1128/IAI.70.7.3973-3977.2002.

38. Galli, F., Battistoni, A., Gambari, R., Pompella, A., Bragonzi, A., Pilolli, F., Iuliano, L., Piroddi, M., Dechecchi, M.C., and Cabrini, G. (2012). Oxidative stress and antioxidant therapy in cystic fibrosis. Biochim Biophys Acta Mol Basis Dis *1822*, 690–713. 10.1016/j.bbadis.2011.12.012.

39. Relja, B., Omid, N., Schaible, A., Perl, M., Meier, S., Oppermann, E., Lehnert, M., and Marzi, I. (2015). Pre- or post-treatment with ethanol and ethyl pyruvate results in distinct anti-

904 inflammatory responses of human lung epithelial cells triggered by interleukin-6. Mol Med
905 Rep *12*, 2991–2998. 10.3892/mmr.2015.3764.

906 40. Hollenbach, M., Hintersdorf, A., Huse, K., Sack, U., Bigl, M., Groth, M., Santel, T., Buchold, M.,
907 Lindner, I., Otto, A., et al. (2008). Ethyl pyruvate and ethyl lactate down-regulate the
908 production of pro-inflammatory cytokines and modulate expression of immune receptors.
909 Biochem Pharmacol *76*, 631–644. 10.1016/j.bcp.2008.06.006.

910 41. Chakhtoura, M., Chain, R.W., Sato, P.Y., Qiu, C.C., Lee, M.H., Meissler, J.J., Eisenstein, T.K.,
911 Koch, W.J., Caricchio, R., and Gallucci, S. (2019). Ethyl pyruvate modulates murine dendritic
912 cell activation and survival through their immunometabolism. Front Immunol *10*, 1–16.
913 10.3389/fimmu.2019.00030.

914 42. Kimura, A., Yamauchi, Y., Hodono, S., Stewart, N.J., Hosokawa, O., Hagiwara, Y., Imai, H., and
915 Fujiwara, H. (2017). Treatment response of ethyl pyruvate in a mouse model of chronic
916 obstructive pulmonary disease studied by hyperpolarized 129Xe MRI. Magn Reson Med *78*,
917 721–729. 10.1002/mrm.26458.

918 43. Min, B.K., Park, S., Kang, H.J., Kim, D.W., Ham, H.J., Ha, C.M., Choi, B.J., Lee, J.Y., Oh, C.J., Yoo,
919 E.K., et al. (2019). Pyruvate dehydrogenase kinase is a metabolic checkpoint for polarization
920 of macrophages to the M1 phenotype. Front Immunol *10*. 10.3389/fimmu.2019.00944.

921 44. Zhang, W., Zhang, S.L., Hu, X., and Tam, K.Y. (2015). Targeting Tumor Metabolism for Cancer
922 Treatment: Is Pyruvate Dehydrogenase Kinases (PDKs) a Viable Anticancer Target? Int J Biol
923 Sci *11*, 1390. 10.7150/IJBS.13325.

924 45. Li, J., Diao, B., Guo, S., Huang, X., Yang, C., Feng, Z., Yan, W., Ning, Q., Zheng, L., Chen, Y., et al.
925 (2017). VSIG4 inhibits proinflammatory macrophage activation by reprogramming
926 mitochondrial pyruvate metabolism. Nat Commun *8*. 10.1038/S41467-017-01327-4.

927 46. McCall, C.E., Zabalawi, M., Liu, T., Martin, A., Long, D.L., Buechler, N.L., Arts, R.J.W., Netea,
928 M., Yoza, B.K., Stacpoole, P.W., et al. (2018). Pyruvate dehydrogenase complex stimulation
929 promotes immunometabolic homeostasis and sepsis survival. JCI Insight *3*.
930 10.1172/jci.insight.99292.

931 47. Chakhtoura, M., Chain, R.W., Sato, P.Y., Qiu, C.C., Lee, M.H., Meissler, J.J., Eisenstein, T.K.,
932 Koch, W.J., Caricchio, R., and Gallucci, S. (2019). Ethyl pyruvate modulates murine dendritic
933 cell activation and survival through their immunometabolism. Front Immunol *10*, 30.
934 10.3389/FIMMU.2019.00030/BIBTEX.

935 48. Meiser, J., Krämer, L., Sapcariu, S.C., Battello, N., Ghelfi, J., D'Herouel, A.F., Skupin, A., and
936 Hiller, K. (2016). Pro-inflammatory macrophages sustain pyruvate oxidation through pyruvate
937 dehydrogenase for the synthesis of itaconate and to enable cytokine expression. Journal of
938 Biological Chemistry *291*, 3932–3946. 10.1074/jbc.M115.676817.

939 49. O'Neill, L.A.J., and Artyomov, M.N. (2019). Itaconate: the poster child of metabolic
940 reprogramming in macrophage function. Nat Rev Immunol *19*, 273–281. 10.1038/S41577-
941 019-0128-5.

942 50. Domínguez-Andrés, J., Novakovic, B., Li, Y., Scicluna, B.P., Gresnigt, M.S., Arts, R.J.W., Oosting,
943 M., Moorlag, S.J.C.F.M., Groh, L.A., Zwaag, J., et al. (2019). The Itaconate Pathway Is a Central
944 Regulatory Node Linking Innate Immune Tolerance and Trained Immunity. Cell Metab *29*,
945 211-220.e5. 10.1016/J.CMET.2018.09.003.

946 51. Bailey, J.D., Diotallevi, M., Nicol, T., McNeill, E., Shaw, A., Chuaiphichai, S., Hale, A., Starr, A.,
947 Nandi, M., Stylianou, E., et al. (2019). Nitric Oxide Modulates Metabolic Remodeling in
948 Inflammatory Macrophages through TCA Cycle Regulation and Itaconate Accumulation. Cell
949 Rep *28*, 218-230.e7. 10.1016/j.celrep.2019.06.018.

950 52. Zhu, X., Long, D., Zabalawi, M., Ingram, B., Yoza, B.K., Stacpoole, P.W., and McCall, C.E.
951 (2020). Stimulating pyruvate dehydrogenase complex reduces itaconate levels and enhances
952 TCA cycle anabolic bioenergetics in acutely inflamed monocytes. J Leukoc Biol *107*, 467–484.
953 10.1002/JLB.3A1119-236R.

954 53. Bartell, J.A., Sommer, L.M., Haagensen, J.A.J., Loch, A., Espinosa, R., Molin, S., and Johansen,
955 H.K. (2019). Evolutionary highways to persistent bacterial infection. Nat Commun *10*, 629.
956 10.1038/s41467-019-08504-7.

957 54. Cavaleiro, A.M., Kim, S.H., Seppälä, S., Nielsen, M.T., and Nørholm, M.H.H. (2015). Accurate
958 DNA assembly and genome engineering with optimized uracil excision cloning. ACS Synth Biol
959 *4*, 1042–1046. 10.1021/acssynbio.5b00113.

960 55. Chen, W., Zhang, Y., Zhang, Y., Pi, Y., Gu, T., Song, L., Wang, Y., and Ji, Q. (2018). CRISPR/Cas9-
961 based genome editing in Pseudomonas aeruginosa and cytidine deaminase-mediated base
962 editing in Pseudomonas species. iScience *6*, 222–231. 10.1016/j.isci.2018.07.024.

963 56. Chen, W., Zhang, Y., Zhang, Y., Pi, Y., Gu, T., Song, L., Wang, Y., and Ji, Q. (2018). CRISPR/Cas9-
964 based genome editing in Pseudomonas aeruginosa and cytidine deaminase-mediated base
965 editing in Pseudomonas species. iScience *6*, 222–231. 10.1016/j.isci.2018.07.024.

966 57. Choi, K.H., and Schweizer, H.P. (2006). mini-Tn7 insertion in bacteria with single attTn7 sites:
967 example Pseudomonas aeruginosa. Nat Protoc *1*, 153–161. 10.1038/NPROT.2006.24.

968 58. Turner, K.H., Wessel, A.K., Palmer, G.C., Murray, J.L., and Whiteley, M. (2015). Essential
969 genome of Pseudomonas aeruginosa in cystic fibrosis sputum. Proc Natl Acad Sci U S A *112*,
970 4110–4115. 10.1073/pnas.1419677112.

971 59. Deschamps, E., Schaumann, A., Schmitz-Afonso, I., Afonso, C., Dé, E., Loutelier-Bourhis, C.,
972 and Alexandre, S. (2021). Membrane phospholipid composition of Pseudomonas aeruginosa
973 grown in a cystic fibrosis mucus-mimicking medium. Biochimica et Biophysica Acta (BBA) -
974 Biomembranes *1863*, 183482. 10.1016/j.bbamem.2020.183482.

975 60. Pedersen, B.H., Gurdo, N., Johansen, H.K., Molin, S., Nikel, P.I., and la Rosa, R. (2021). High-
976 throughput dilution-based growth method enables time-resolved exo-metabolomics of
977 Pseudomonas putida and Pseudomonas aeruginosa. Microb Biotechnol *0*, 1–13.
978 10.1111/1751-7915.13905.

979 61. Bartell, J.A., Sommer, L.M., Haagensen, J.A.J., Loch, A., Espinosa, R., Molin, S., and Johansen,
980 H.K. (2019). Evolutionary highways to persistent bacterial infection. Nat Commun *10*, 629.
981 10.1038/s41467-019-08504-7.

982 62. Walters, M.S., Gomi, K., Ashbridge, B., Moore, M.A.S., Arbelaez, V., Heldrich, J., Ding, B.-S.,
983 Rafii, S., Staudt, M.R., and Crystal, R.G. (2013). Generation of a human airway epithelium
984 derived basal cell line with multipotent differentiation capacity. Respir Res *14*, 135.
985 10.1186/1465-9921-14-135.

986 63. Kumar, S., Stecher, G., Li, M., Knyaz, C., and Tamura, K. (2018). MEGA X: Molecular
987 Evolutionary Genetics Analysis across computing platforms. Mol Biol Evol, 1547–1549.

988 64. Callister, S.J., Barry, R.C., Adkins, J.N., Johnson, E.T., Qian, W.J., Webb-Robertson, B.J.M.,
989 Smith, R.D., and Lipton, M.S. (2006). Normalization approaches for removing systematic
990 biases associated with mass spectrometry and label-free proteomics. J Proteome Res *5*, 277–
991 286. 10.1021/PR050300L.

992